Article

BRD9-mediated chromatin remodeling suppresses osteoclastogenesis through negative feedback mechanism

Jiahui Du [1,2,3,4], Yili Liu[1,2,3,4], Xiaolin Wu[1,2,3,4], Jinrui Sun[1,2,3], Junfeng Shi[1,2,3], Hongming Zhang[1,2,3], Ao Zheng[1,2,3], Mingliang Zhou [1,2,3] ✉ & Xinquan Jiang [1,2,3] ✉

Bromodomain-containing protein 9 (BRD9), a component of non-canonical BAF chromatin remodeling complex, has been identified as a critical therapeutic target in hematological diseases. Despite the hematopoietic origin of osteoclasts, the role of BRD9 in osteoclastogenesis and bone diseases remains unresolved. Here, we show *Brd9* deficiency in myeloid lineage enhances osteoclast lineage commitment and bone resorption through downregulating interferon-beta (IFN-β) signaling with released constraint on osteoclastogenesis. Notably, we show that BRD9 interacts with transcription factor FOXP1 activating *Stat1* transcription and IFN-β signaling thereafter. Besides, function specificity of BRD9 distinguished from BRD4 during osteoclastogenesis has been evaluated. Leveraging advantages of pharmacological modulation of BRD9 and flexible injectable silk fibroin hydrogel, we design a local deliver system for effectively mitigating zoledronate related osteonecrosis of the jaw and alleviating acute bone loss in lipopolysaccharide-induced localized aggressive periodontitis. Overall, these results demonstrate the function of BRD9 in osteoclastogenesis and its therapeutic potential for bone diseases.

The function and homeostasis of bone relies on the balanced bone remodeling process, which is a continuously cycle of bone formation mediated by osteoblasts and resorption mediated by osteoclasts throughout life. The bone remodeling process is under sophisticatedly orchestrated with their imbalance can disturb the skeletal architecture and cause debilitating bone diseases such as osteoporosis, osteopetrosis, osteonecrosis, Paget's disease and so on[1].

Osteoclasts are hematopoietic myeloid lineage and derived from bone marrow-derived monocytes (BMDMs). In the last decades, it is quite well-documented that osteoclastogenesis is initiated with receptor activator of nuclear factor κB (NF-κB) ligand (RANKL) and macrophage colony stimulating factor (M-CSF) in the bone microenvironment[2]. Afterward, it is followed by a series of activation, proliferation, fusion and maturation process, then the terminally differentiated multinucleated osteoclasts are able to secrete proteases and acids, such as tartrate resistant acid phosphatase (TRAP), cathepsin K (CTSK) and matrix metallopeptidase 9 (MMP9), conducting their bone resorptive activity[3].

The above osteoclast lineage commitment and differentiation are sophisticatedly regulated by complex signal transduction cascades that converge to transcriptional modulation[4]. Mammalian BRG1-associated factors (BAF) complex is ATP-dependent chromatin remodelers comprising multiple protein subunits that translocate nucleosome and regulate gene transcription with DNA-binding factors[5,6].

[1]Department of Prosthodontics, Shanghai Ninth People's Hospital, Shanghai Jiao Tong University School of Medicine, Shanghai 200011, China. [2]College of Stomatology, Shanghai Jiao Tong University, Shanghai 200011, China. [3]National Center for Stomatology, National Clinical Research Center for Oral Diseases, Shanghai Key Laboratory of Stomatology, Shanghai Research Institute of Stomatology, Shanghai Engineering Research Center of Advanced Dental Technology and Materials, Shanghai 200011, China. [4]These authors contributed equally: Jiahui Du, Yili Liu, Xiaolin Wu. ✉e-mail: mingliangzhou@aliyun.com; xinquanjiang@aliyun.com

Multiple lines of evidence indicate that the BAF complex plays essential roles for controlling expression of genes linked to hematopoietic developmental processes at promoter and enhancer regions, alongside its better-known function in suppressing a variety of cancers in humans[5,7,8]. In particular, bromodomain-containing protein 9 (BRD9), a crucial component of the distinct non-canonical BAF (ncBAF) complex, was identified to exert a prominent function during myeloid lineage development[9–11]. For example, acute myeloid leukemia appears to be specific-dependent on the BRD9-containing BAF complex via the activation of STAT5 pathway[11]. By targeting BRD9, AML cells undergo cell cycle arrest and differentiate, suggesting BRD9 as an essential therapeutic target in leukemia[10]. Besides, it has been established that BRD9 regulates interferon-stimulated genes (ISGs) during macrophage activation via cooperation with BET protein BRD4 and also acts a modulator of glucocorticoid responses[12,13]. These observations suggested that BRD9 is crucial during myeloid lineage determination as well as macrophage inflammatory response. Osteoclasts are myeloid origin and share the common ancestor with macrophage in the hematopoietic lineage. However, there was little evidence for the association between BRD9-mediated chromatin remodeling and osteoclast lineage differentiation in bone homeostasis.

Here, we report that the gene expression of BRD9 is upregulated during RANKL-induced osteoclast differentiation. *Brd9* deficiency in myeloid lineage enhanced osteoclast lineage commitment and bone resorption through downregulating interferon-beta (IFN-β) signaling with released constraint on osteoclastogenesis. Notably, we show that BRD9 interacts with transcription factor (TF) FOXP1 and activates *Stat1* transcription and IFN-β signaling thereafter. Besides, function specificity of BRD9 distinguished from BRD4 during osteoclastogenesis were evaluated. Leveraging the advantages of pharmacological modulation of BRD9 and flexible injectable silk fibroin hydrogel, we designed a local deliver system for effectively mitigating zoledronate (ZOL)-related osteonecrosis of the jaw (ONJ) and acute bone loss in lipopolysaccharide (LPS)-induced localized aggressive periodontitis. In summary, these findings indicate that BRD9-FOXP1-STAT1 axis is crucial for the negative feedback signaling in osteoclastogenesis, expand our knowledge of the intricate interactions among chromatin remodelers, transcription factors, and signaling pathways in bone homeostasis and also highlight its therapeutic potential for bone diseases.

Results

Loss of *Brd9* in myeloid lineage leads to less bone mass

To investigate the critical role of BRD9 in osteoclastogenesis, we examined its expression pattern in osteoclast lineage cell. We found that BRD9 is high expressed in CTSK + osteoclasts on the surface of trabecular bone of distal femur from the 4-week-old mouse (Fig. 1a). Moreover, BMDMs were cultured with M-CSF and RANKL to further evaluate the expression level of BRD9 during proliferation, differentiation, and maturation stages at indicated days (Fig. 1b). We found that BRD9 expression was gradually upregulated after RANKL treatment both at mRNA and protein level during the osteoclastogenesis (Fig. 1c, d), which is also well visualized in the immunofluorescent staining of BRD9 in BMDMs after RANKL-induction in vitro (Fig. 1e).

To further determine whether BRD9 plays a crucial role during osteoclastogenesis, we generated knockout mice through specific deletion of BRD9 in the osteoclast lineage. Mice bearing *loxP* sites encompassing the *Brd9 exon6-exon7* (*Brd9*^{fl/fl} mice) were crossed with a myeloid-specific *Cre*-recombinase (*Cre*)-expressing mouse line, those expressing Cre driven by the lysozyme M promoter (*LysM-Cre* mice). Mice lacking *Brd9* in *LysM*-Cre-expressing cells, hereafter referred to as *LysM-Cre;Brd9*^{fl/fl} mice (Supplementary Fig. 1a). It showed that BRD9 were knocked out efficiently at both mRNA and protein levels in BMDMs from *LysM-Cre;Brd9*^{fl/fl} mice (Supplementary Fig. 1b, c).

In μCT analysis, *LysM-Cre;Brd9*^{fl/fl} mice exhibited decreased femoral trabecular bone mass compared to control mice at 4 weeks of

age, with decreased bone volume/tissue volume ratio (BV/TV), bone volume/tissue volume ratio (BS/TV), trabecular thickness (Tb.Th), trabecular number (Tb.N), bone mineral density (BMD) and increased bone surface/volume ratio (BS/BV), trabecular separation (Tb.Sp) and porosity percent (Po). *LysM-Cre;Brd9*^{fl/fl} mice also exhibited decreased cortical thickness at 4 weeks of age, with decreased cross sectional bone area (Ct.Ar) and perimeter (Ct.Pm) (Fig. 1f, g). Histologically, the H&E staining (Fig. 1h) and Von Kossa staining (Fig. 1i) results showed the decreased bone mass and mineralization in the distal femurs after *Brd9* loss in myeloid cell lineage compared with littermate control mice at 4 weeks of age.

Brd9 deletion enhances osteoclast lineage commitment in vivo

To investigate the cellular mechanism accounting for the decreased bone mass after *Brd9* loss in myeloid cell lineage, we examined osteoclastic bone resorption and osteoblastic bone formation individually. We found that the number and size of TRAP-positive differentiated osteoclasts were increased on the bone surface of the femurs from *LysM-Cre;Brd9*^{fl/fl} mice at 4 weeks of age (Fig. 2a, b). Furthermore, using Tdt as a reporter to trace the myeloid cell fate, we found that the cell number of CTSK + osteoclasts from *LysM* + myeloid lineage (Tdt +CTSK + cell) was increased apparently on the bone surface of the femurs in the mutant mice compared to control mice at 4 weeks of age, suggesting enhanced osteoclast lineage commitment and bone resorption after loss of *Brd9* (Fig. 2c, d).

To determine if the osteoblastic bone formation is also affected in *LysM-Cre;Brd9*^{fl/fl} mice, we investigate the expression of alkaline phosphatase (ALP) (Fig. 2e) and the number of RUNX2 + osteoblasts on the trabecular bone surface at 4 weeks of age (Fig. 2f). It was showed that the number of osteoblasts and osteoblastic osteogenic activity was comparable between *LysM-Cre;Brd9*^{fl/fl} mice and littermate control mice. We then assessed the mineral apposition on the bone surface dynamically with calcein/Alizarin Red S (ARS) labeling. The results showed that the bone formation rate was comparable while more eroded bone surface was observed in *LysM-Cre;Brd9*^{fl/fl} mice compared with littermate control mice at 4 weeks of age (Fig. 2g).

Thus, it is conceivable that the enhanced osteoclast lineage commitment following *Brd9* ablation accelerates bone resorption, leading to excessive bone mass loss.

BRD9 suppresses RANKL-induced osteoclast differentiation in vitro

Furthermore, the BMDMs from *LysM-Cre;Brd9*^{fl/fl} and control mice at 4 weeks of age were administered with RANKL for osteoclastic induction in vitro. In line with the role of BRD9 in vivo, we found that an increased number and larger size of TRAP + multinuclear cells from *Brd9* depleted BMDMs than that from control BMDMs after 3 days of RANKL-induction (Fig. 3a). And the expression of osteoclastic-specific genes of *Acp5*, *Ctsk*, and *Mmp9* were increased in BMDMs from *LysM-Cre;Brd9*^{fl/fl} mice compared with that from control littermates (Fig. 3b, c).

The function of BRD9 during osteoclastogenesis is also investigated with a selective cellular chemical inhibitor for BRD9, iBRD9[14,15]. IBRD9 treatment in BMDMs leads to dose-dependent increase on the gene expression of *Acp5* and *Mmp9* in osteoclastic induced BMDMs after 24 h, without apparent cell toxicity under the concentration of 9 μM (Fig. 3d, e). Consistently, we also confirmed the dose-dependent increase on the number and size of TRAP + multinuclear differentiated osteoclasts from RANKL-induced BMDMs with iBRD9 treatment (Fig. 3f). The concentration of 1 μM iBRD9 was chosen in the further studies for its most prominent function on promoting osteoclastogenesis.

To further investigate whether BRD9 inhibitor could induce osteoclastogenesis alone or function under RANKL-induction, we compared the protein expression of FOS, CTSK, as well as the mRNA
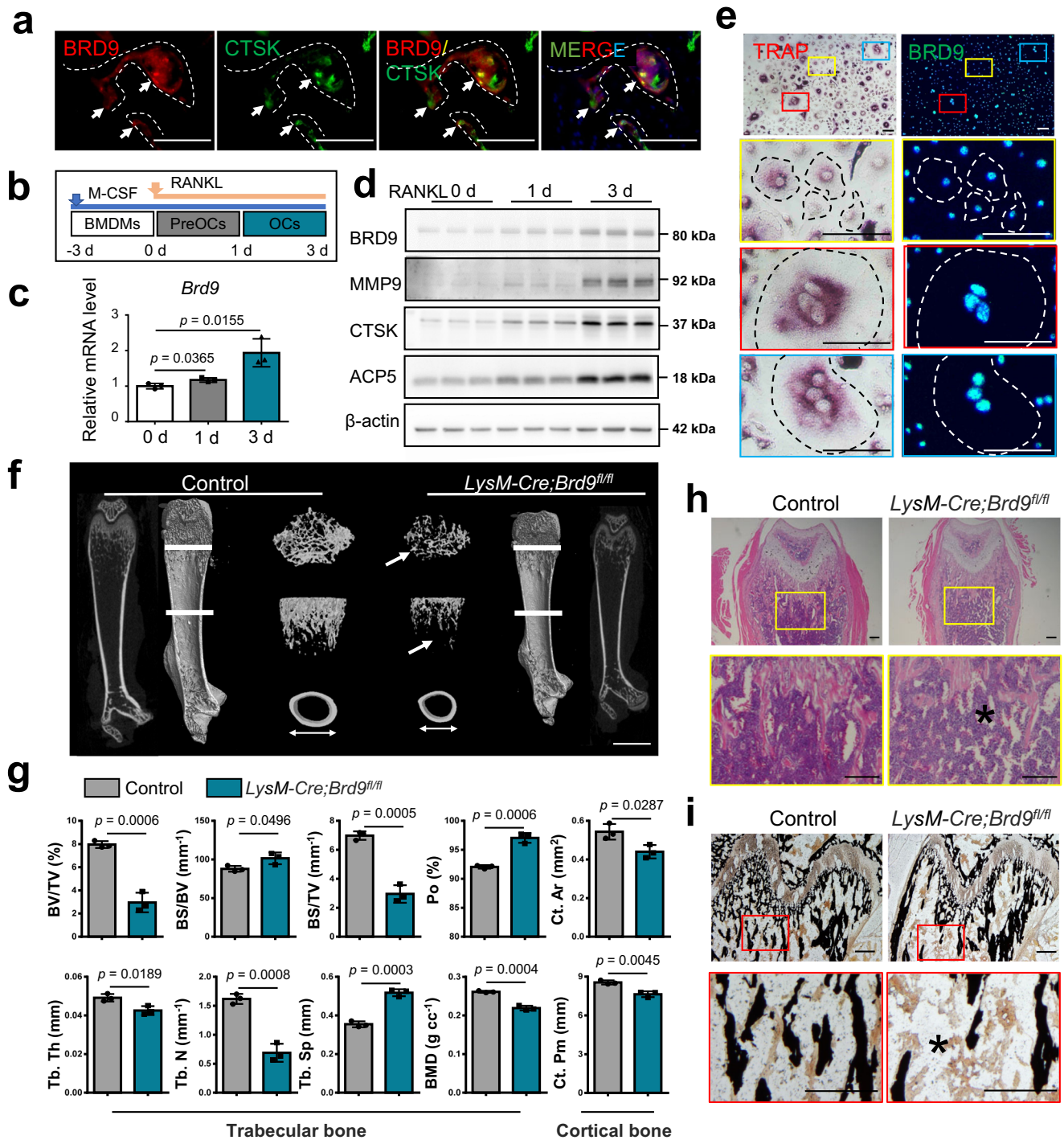
Fig. 1 | Loss of *Brd9* in myeloid lineage leads to less bone mass.
a Immunofluorescence staining of BRD9 (red) and CTSK (green) in the mouse distal femur at 4 weeks of age. White dashed lines outline the surface of trabecular bone. Scale bar, 100 μm. **b** Schema for osteoclastic differentiation stages of BMDMs in vitro. Bone marrow-derived monocytes, BMDMs, osteoclast precursors, preOCs, and matured osteoclast, OCs. **c** *Brd9* mRNA expression in BMDMs at indicated days after RANKL-induction, as measured by qPCR. *n* = 3 biologically independent samples. **d** BRD9, MMP9, CTSK and ACP5 protein expression in BMDMs at indicated days after RANKL-induction. **e** Immunofluorescence staining of BRD9 (green) and TRAP staining (red) in BMDMs after 3 days of RANKL-induction. Colored boxes in the first panel are shown at higher magnification in below. Dashed lines outline the cell boundaries. Scale bar, 100 μm. **f** Representative micro-CT image of the distal trabecular bone and cortical bone of femurs from 4-week-old *LysM-Cre;Brd9^fl/fl^* mice and littermate control mice. Arrows indicates the decreased bone mass. Scale bar,

2 mm. **g** Quantification analysis of bone volume/tissue volume ratio (BV/TV), bone surface/volume ratio (BS/BV), bone volume/tissue volume ratio (BS/TV), porosity percent (Po), trabecular thickness (Tb. Th), trabecular number (Tb. N), trabecular separation (Tb. Sp), bone mineral density (BMD), cortical crossectional bone area (Ct. Ar) and perimeter (Ct. Pm) of femurs from 4-week-old *LysM-Cre;Brd9^fl/fl^* mice and littermate control mice. *n* = 3. **h** H&E staining of femurs from 4-week-old *LysM-Cre;Brd9^fl/fl^* mice and littermate control mice. Box in the first panel is shown at higher magnification in below. Asterisk indicates the decreased bone mass. Scale bar, 200 μm. **i** Von Kossa staining of femurs from 4-week-old *LysM-Cre;Brd9^fl/fl^* mice and littermate control mice. Box in the first panel is shown at higher magnification in below. Asterisk indicates the decreased bone mineralization. Scale bar, 200 μm. All data in this figure are represented as mean ± SD. Two-tailed Student's *t*-test for (**c**) and (**g**). All experiments were performed in triplicates unless otherwise stated. Source data are provided in the Source data file.
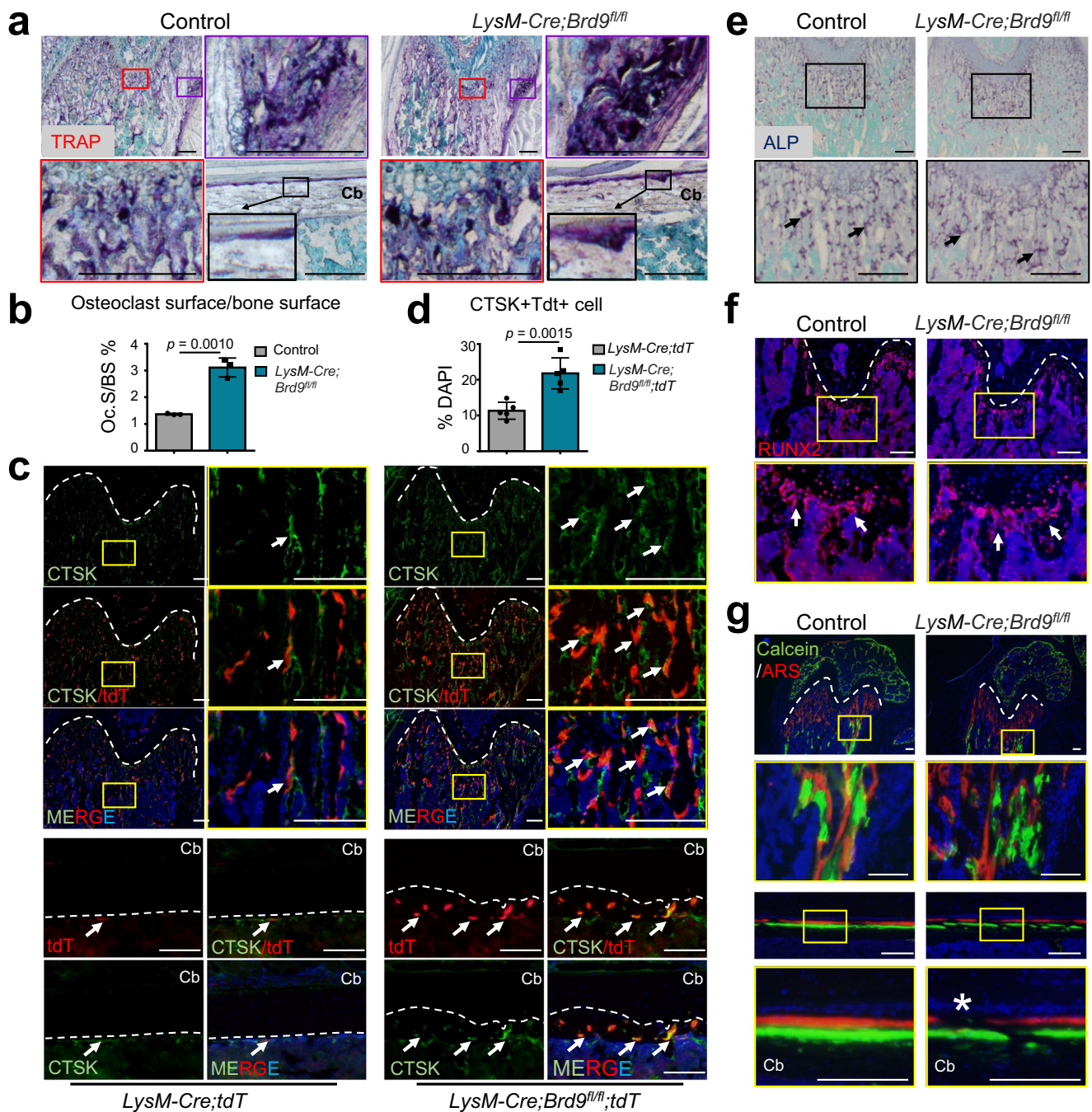
Fig. 2 | Loss of *Brd9* in myeloid lineage leads to enhanced osteoclast lineage commitment in vivo. a TRAP staining of distal trabecular and cortical bone of femurs from 4-week-old *LysM-Cre;Brd9*fl/fl mice and littermate control mice. Colored box in the top left corner is shown at higher magnification in right and below. Cortical bone, Cb. Scale bar, 200 μm. **b** Quantitative analysis of the TRAP + osteoclast surface/bone surface ratios (Oc.S/BS) in the femurs from 4-week-old *LysM-Cre;Brd9*fl/fl mice and littermate control mice. *n* = 3. **c** CTSK immunofluorescence (green) and visualization of tdTomato (red) of femurs from 4-week-old *LysM-Cre;Brd9*fl/fl;*tdT* mice and littermate control mice. Box in the left is shown at higher magnification in right. The progeny of the myeloid lineage shows red signal. Arrows indicate double positive signals. White dashed lines outline the growth plate of distal femur. Cortical bone, Cb. Scale bar, 200 μm. **d** Quantitative analysis of the ratio of CTSK + tdT+ myeloid lineage osteoclasts in the femurs from 4-week-

old *LysM-Cre;Brd9*fl/fl;*tdT* mice and littermate control mice. *n* = 5. **e** ALP staining (purple) of distal femur from *LysM-Cre;Brd9*fl/fl mice and littermate control mice at 4 weeks of age. Arrows indicate positive signals. Scale bar, 200 μm. **f** RUNX2 immunofluorescence (red) of distal femur from *LysM-Cre;Brd9*fl/fl mice and littermate control mice at 4 weeks of age. Arrows indicate RUNX2-positive osteoblasts. White dashed lines outline the growth plate of distal femur. Scale bar, 200 μm. **g** visualization of calcein/ Alizarin Red S (ARS) labeling in *LysM-Cre;Brd9*fl/fl mice and littermate control mice at age of 4 weeks. Asterisk indicates the eroded bone surface. White dashed lines outline the growth plate of distal femur. Cortical bone, Cb. Scale bar, 200 μm. All data in this figure are represented as mean ± SD. Two-tailed Student's *t*-test for (**b**) and (**d**). All experiments were performed in triplicates unless otherwise stated. Source data are provided in the Source data file.
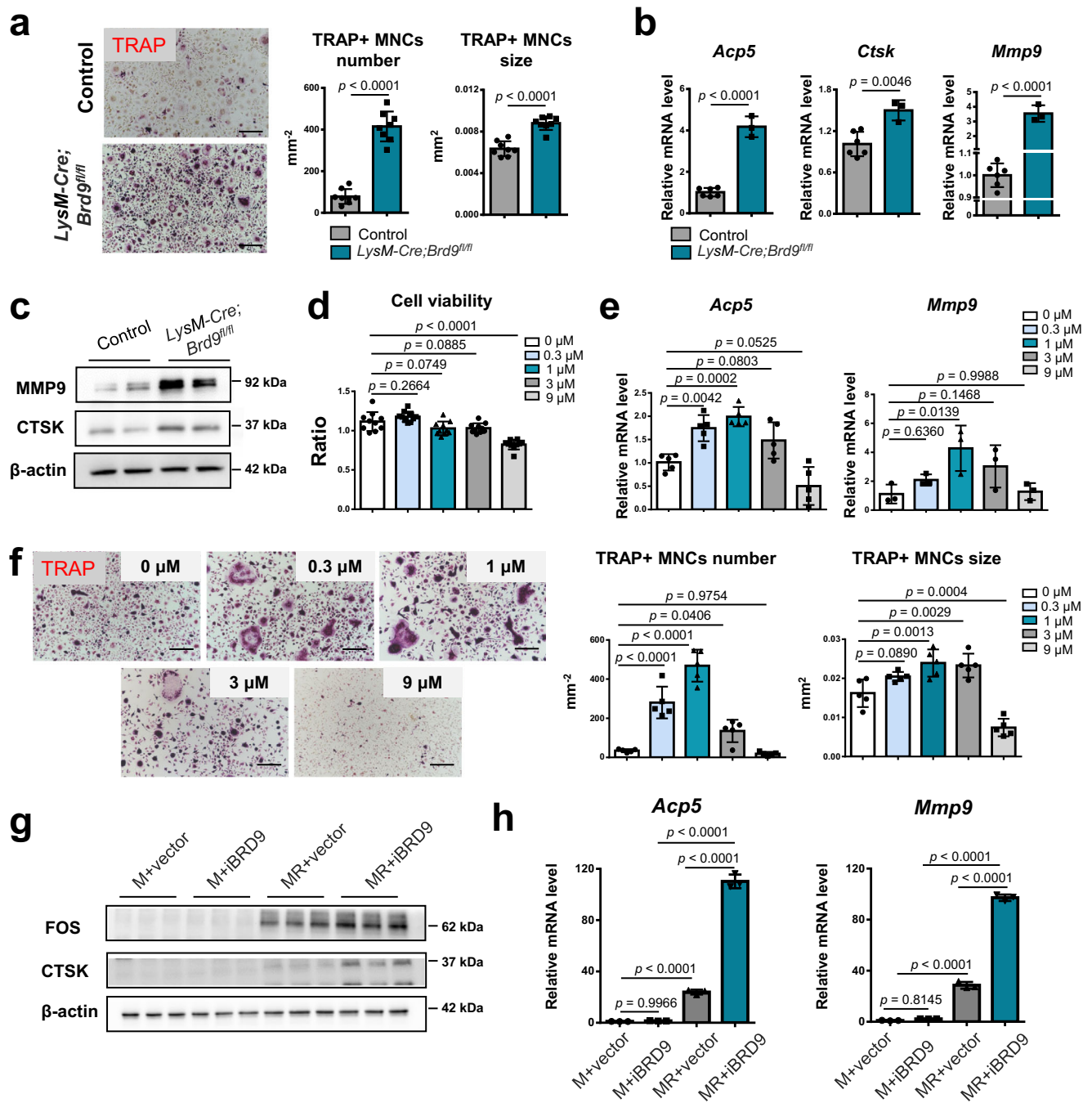
Fig. 3 | BRD9 deletion and inhibition in BMDMs leads to overactivated osteoclastogenesis in vitro. a TRAP staining and quantification analysis of BMDMs from 4-week-old *LysM-Cre;Brd9^fl/fl* mice and littermate control mice after 3 days of RANKL-induction. Scale bar, 200 μm. *n* = 8. **b** The mRNA expression of osteoclastic-specific genes of *Acp5, Ctsk,* and *Mmp9* in BMDMs from *LysM-Cre;Brd9^fl/fl* mice compared with that from control littermates after 3 days of RANKL-induction, as measured by qPCR. *n* = 3 for *LysM-Cre;Brd9^fl/fl* mice group. *n* = 6 for control littermates. **c** The protein expression of MMP9 and CTSK in BMDMs from *LysM-Cre;Brd9^fl/fl* mice compared with that from control littermates after 3 days of RANKL-induction, as measured by western blot. **d** Cell viability of RANKL-induced BMDMs with 1 day of iBRD9 at different concentration, shown by cell counting kit 8 assay. *n* = 10 biologically independent samples. **e** The mRNA expression of *Acp5* and *Mmp9* in RANKL-induced BMDMs with 1 day of iBRD9 at different concentration, as measured by qPCR. *n* = 5 biologically independent samples for *Acp5*. *n* = 3

biologically independent samples for *Mmp9*. **f** TRAP staining and quantification analysis of RANKL-induced BMDMs with 5 days of iBRD9 at different concentration. Scale bar, 200 μm. *n* = 5 biologically independent samples. **g** The protein expression of FOS and CTSK in BMDMs after 3 days of 1 μM iBRD9 or vector treatment with or without RANKL-induction, as measured by western blot. M-CSF, M; RANKL, R. **h** The mRNA expression of *Acp5* and *Mmp9* in BMDMs after 3 days of 1 μM iBRD9 or vector treatment with or without RANKL-induction, as measured by qPCR. M-CSF, M; RANKL, R. *n* = 3 biologically independent samples. All data in this figure are represented as mean ± SD. Two-tailed Student's *t*-test for (**a**) and (**b**). One-way analysis of variance (ANOVA) with Dunnett's multiple comparisons test for (**d**), (**e**), and (**f**); ANOVA with Tukey's multiple comparisons test for (**h**). All experiments were performed in triplicates unless otherwise stated. Source data are provided in the Source data file.

expression of *Acp5* and *Mmp9* in BMDMs after 1 μM iBRD9 or vector treatment with or without RANKL-induction. We found that BRD9 inhibitor exert no apparent effect on osteoclastogenesis without RANKL-induction, suggesting the function of BRD9 is RANKL-dependent (Fig. 3g, h).

Taken together, these findings suggest that BRD9, which was upregulated after RANKL treatment, exerts suppressing regulation on RANKL-induced osteoclast differentiation in a negative feedback mechanism, and both genetic deletion and inhibition of BRD9 in BMDMs consistently promotes osteoclast differentiation.

BRD9 suppresses osteoclastogenesis via interferon-beta signaling

To further investigate the feedback mechanism of BRD9-mediated suppression on RANKL-induced osteoclast differentiation, we conducted mRNA sequencing to compare the transcription profile in BMDMs after 1 day of BRD9 inhibition during osteoclastic differentiation with M-CSF and RANKL, refer as MR + iBRD9, with the control group (MR + vector). The RNA-sequencing data showed well-separated gene expression patterns between two groups with a total of 211 downregulated and 184 upregulated genes in BMDMs in MR + iBRD9 group (fold change > = 1.2; $p < 0.05$), as shown in the heatmap and MA plot (Fig. 4a). The 10 top gene ontology (GO) biological process terms in the comparison between BMDMs in MR + vector and MR + iBRD9 group, are intensely enriched on defense response, response to interferon-beta (IFN-β) and external stimulus, and immune system process and their topological relationships illustrated in a directed acyclic graph (DAG) (Fig. 4b and Supplementary Fig. 2). Gene set enrichment analysis (GSEA) further revealed that the IFN-β response, acetylcholine receptor signaling, and immune receptor activity were significantly downregulated, while ribosome biogenesis, synaptic transmission, and rRNA processing were upregulated in MR + iBRD9 group (Fig. 4c, d).

Thereinto, IFN-β signaling activity, as one of the top downregulated signaling pathways after BRD9 inhibition, is reported to activate ISGs through interferon-stimulated gene factor 3 (ISGF3), which consists of activated signal transducer and activator of transcription 1 (STAT1), signal transducer and activator of transcription 2 (STAT2), and interferon regulatory factors[16]. Previous studies have shown that global IFN-β-knockout mice display an osteoporotic phenotype due to an excessive osteoclastogenesis[17]. In our present study, we identified that RANKL activates the IFN-β signaling with increased IFN-β, STAT1, STAT2 during osteoclastogenesis (Fig. 4e), which synchronizes with the expression profile of BRD9 (Fig. 1c, d). While IFN-β signaling activity was downregulated in RANKL-induced BMDMs after iBRD9 treatment (Fig. 4f). Therefore, we presumed that the transcriptional downregulated IFN-β signaling in BMDMs may, at least partially, contribute to the excessive osteoclastogenesis after BRD9 inhibition. To verify this hypothesis, we added IFN-β1 cytokine into BRD9 inhibited BMDMs, and found that the increased osteoclastogenesis after BRD9 inhibition was rescued after IFN-β signaling upregulation, as shown with the downregulated expression of osteoclastogenic genes of *Acp5* and *Mmp9* (Fig. 4g), and the decreased number and size of TRAP + differentiated osteoclasts (Fig. 4h).

Since it is reported that glucocorticoid/dexamethasone (DEX) promotes osteoclastogenesis[18], and BRD9 inhibition attenuated macrophage inflammation by synergizing with glucocorticoid response[13], the potential synergizing function of BRD9 inhibition and glucocorticoid signaling during osteoclastogenesis has been further analyzed. The results have shown that DEX promotes osteoclastogenesis at the concentration of 10^{-9} M, with no significant promotion below the concentration of 10^{-10} M. While the low DEX dose showed promotion on osteoclastogenesis when combined with iBRD9 at 0.1 μM, the low concentration exerting no apparent effect on osteoclastogenesis alone (Supplementary Fig. 3a, b). Then we conducted mRNA sequencing

analysis to unveil the change on gene transcription profile after synergistic 0.1 μM iBRD9/10^{-10} M DEX treatment during osteoclastogenesis. Besides of the apparent activation on osteoclast-related genes (Supplementary Fig. 3c), the enriched top ten changed signaling pathways in iBRD9/DEX-treated group compared with the control group were listed (Supplementary Fig. 3d). We noticed the functional categories of iBRD9/DEX cooperatively regulated genes were enriched on metabolic process, electron transport chain, and peptide biosynthetic process during osteoclastogenesis. The regulatory mechanisms differ from 1 μM iBRD9-alone regulated gene network, which enriched in response to IFN-β signaling and external stimulus mentioned above, and also differ from the finding in macrophage activation that the synergistic gene signature is enriched in inflammatory responses categories[13]. This finding suggests that BRD9 modulated regulatory mechanism is characterized with context-dependency and cell type-specificity.

In summary, we conclude that the transcriptional activation on IFN-β signaling in BMDMs may contribute to BRD9-mediated negative feedback during osteoclastogenesis.
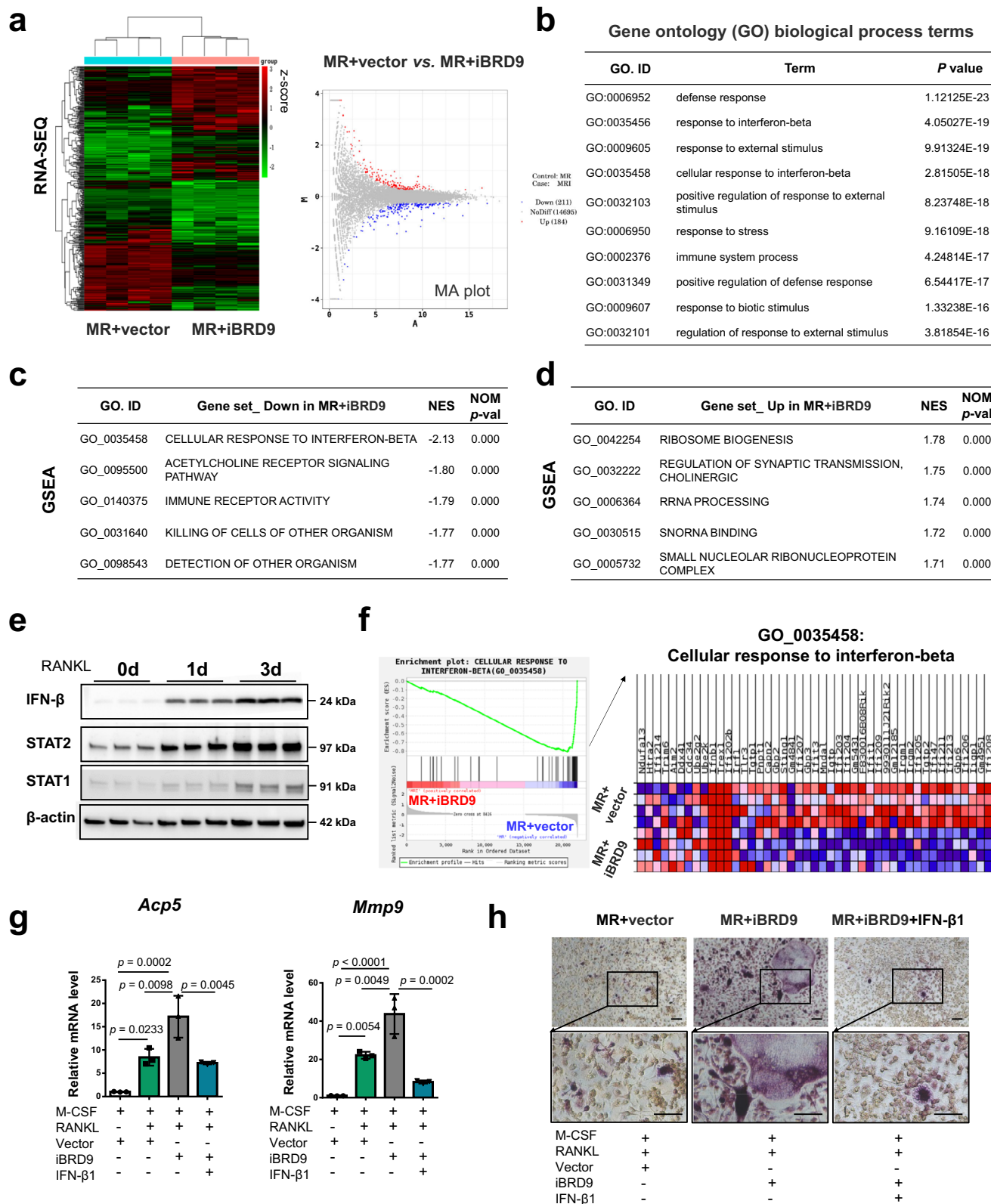
Stat1 is critical for BRD9-mediated osteoclastogenesis suppression

To further elucidate how BRD9 participates in the transcriptional regulation during the negative feedback of RANKL-induced osteoclastogenesis, we compared RANKL-induced, iBRD9-inhibited gene transcription with the binding profile of BRD9 in BMDMs during osteoclastogenesis using immunoprecipitation (ChIP) sequencing analysis.

There are 717 genes, where BRD9 binding, RANKL-induced while downregulated after BRD9 inhibition (Fig. 5a). KEGG enrichment analysis of above genes unveiled that the critical transcriptional regulations of BRD9 were enriched on signal transduction, signaling molecules, and interaction as well as immune response (Fig. 5b). The protein-protein interaction (PPI) analysis further identified several crucial hub genes among the gene list, suggesting their potential direct downstream targets of BRD9 during the negative feedback regulation during osteoclastogenesis (Fig. 5c). Thereinto, we noticed STAT1, as one of the hub genes with most interaction numbers and a primary mediator for IFN-β signaling activity[19], is increased after RANKL-induction and expressed in osteoclasts in vivo and in vitro (Figs. 4e, 5d, e). While the gene expression of *Stat1* was downregulated in BMDMs from *LysM-Cre;Brd9^{fl/fl}* mice compared with that from control littermates after RANKL-induction (Fig. 5f) and also downregulated in BMDMs from wild-type mice after BRD9 inhibition (Fig. 5g and h). Previous studies have identified that STAT1, as an important factor involved in osteoporosis, is importance for bone metabolism[19,20]. It has been observed that excessive osteoclastogenesis existed in the bone of the *Stat1*-deficient mice, suggesting its negative regulation of osteoclast differentiation[21]. Therefore, we hypothesized that Stat1 is one of the critical downstream targets in BRD9-mediated negative feedback during osteoclastogenesis.

Mouse macrophage cell line RAW264.7 is a preferred model for molecular mechanism study on osteoclastogenesis[22]. Therefore, we constructed the STAT1 constituently expressed RAW264.7 cell line using lentivirus vector for further function test of iBRD9 inhibitor (Fig. 5i). We found that the expression of osteoclastic-related genes, such as *Mmp9* and *Acp5*, were comparable between control and iBRD9 inhibitor treated *Stat1*-overexpressed RAW264.7 cells, while increased apparently in control-lentivirus transfected RAW264.7 cells after BRD9 inhibition (Fig. 5j). These findings suggest that the downregulated expression of *Stat1* might be a key process in BRD9 inhibition mediated excessive osteoclastogenesis.

Previous studies have indicated that BAF complex plays essential roles for controlling expression of genes linked to developmental

a

b

Gene ontology (GO) biological process terms

GO. ID	Term	*P* value
GO:0006952	defense response	1.12125E-23
GO:0035456	response to interferon-beta	4.05027E-19
GO:0009605	response to external stimulus	9.91324E-19
GO:0035458	cellular response to interferon-beta	2.81505E-18
GO:0032103	positive regulation of response to external stimulus	8.23748E-18
GO:0006950	response to stress	9.16109E-18
GO:0002376	immune system process	4.24814E-17
GO:0031349	positive regulation of defense response	6.54417E-17
GO:0009607	response to biotic stimulus	1.33238E-16
GO:0032101	regulation of response to external stimulus	3.81854E-16

c

GO. ID	Gene set_ Down in MR+iBRD9	NES	NOM *p*-val
GO_0035458	CELLULAR RESPONSE TO INTERFERON-BETA	-2.13	0.000
GO_0095500	ACETYLCHOLINE RECEPTOR SIGNALING PATHWAY	-1.80	0.000
GO_0140375	IMMUNE RECEPTOR ACTIVITY	-1.79	0.000
GO_0031640	KILLING OF CELLS OF OTHER ORGANISM	-1.77	0.000
GO_0098543	DETECTION OF OTHER ORGANISM	-1.77	0.000

d

GO. ID	Gene set_ Up in MR+iBRD9	NES	NOM *p*-val
GO_0042254	RIBOSOME BIOGENESIS	1.78	0.000
GO_0032222	REGULATION OF SYNAPTIC TRANSMISSION, CHOLINERGIC	1.75	0.000
GO_0006364	RRNA PROCESSING	1.74	0.000
GO_0030515	SNORNA BINDING	1.72	0.000
GO_0005732	SMALL NUCLEOLAR RIBONUCLEOPROTEIN COMPLEX	1.71	0.000

e

f

GO_0035458: Cellular response to interferon-beta

g

h

processes at promoter and enhancer regions[7,9]. It is also reported that the 5.5 kb upstream regulatory region of the mouse *Stat1* gene enriches with similar epigenetic signatures with proximal promoter region, functioning as a transcriptional enhancer and conserved among mammals[23]. To further validate the transcriptional regulation of BRD9 on *Stat1*, we cloned the predicted proximal promoter (2.6 kb, −1995 ~ +575) and the enhancer (1.2 kb, −6338 ~ −5138) region of *Stat1* into the PGL3-basic vector to drive the expression of luciferase reporter (Supplementary Fig. 4). We found that the *Stat1* proximal promoter construct in the presence of upstream enhancer region exhibited greater reporter activities than the *Stat1* proximal promoter alone, while BRD9 inhibition repressed the transcription activity of both *Stat1* promoter and enhancer apparently (Fig. 5k). Then, we conducted ChIP-qPCR in osteoclastic induced RAW264.7 cells and validated BRD9 could bind to the promoter and the enhancer of *Stat1* directly (Fig. 5l, Supplementary Fig. 4).

Fig. 4 | BRD9-mediated transcriptional activation of interferon-beta signaling negative regulates osteoclastogenesis. a Heatmap hierarchical clustering and the MA plot showing the gene expression profiles in BMDMs after 1 day of BRD9 inhibition during osteoclastic differentiation with M-CSF and RANKL (MR). $n = 4$. Color scale represents normalized gene FPKM value by z-score scheme. **b** The top 10 Gene ontology (GO) biological process enriched in the comparison between BMDMs in MR + vector and MR + iBRD9 group. **c** Gene set enrichment analysis (GSEA) analysis of the top downregulated gene sets in MR + iBRD9 group compared with control group. **d** GSEA analysis of the top upregulated gene sets in MR + iBRD9 group compared with control group. **e** The protein expression of IFN-β, STAT2, and STAT1 in BMDMs at different days after osteoclastic differentiation, as measured by western blot. **f** GSEA plots and heatmap hierarchical clustering of GO term_0035458 in MR + iBRD9 group and control group. $n = 4$. **g** The mRNA expression of *Acp5* and *Mmp9* in BMDMs treated with 2 days of 1 μM iBRD9 and 0.0625 ng/ml IFN-β1 during osteoclastic induction, as measured by qPCR. $n = 3$ biologically independent samples. **h** TRAP staining of BMDMs treated with 3 days of 1 μM iBRD9 and 0.0625 ng/ml IFN-β1 during osteoclastic induction. Scale bar, 200 μm. All data in this figure are represented as mean ± SD. Hypergeometric distribution test for (**b**). Empirical phenotype-based permutation test for (**c**) and (**d**). One-way analysis of variance (ANOVA) with Tukey's multiple comparisons test for (**g**). All experiments were performed in triplicates unless otherwise stated. Source data are provided in the Source data file.

Mutations in *STAT1* gene have been shown to be in association with multifocal osteomyelitis in patients with Mendelian susceptibility to mycobacterial disease (MSMD), due to impaired inhibition of osteoclast differentiation and bone resorption[24,25]. We also detected there are multiple protein-altering variants, splice site variants and non-coding transcript or untranslated region variants in above predicted promoter and enhancer region of *Stat1*, from the European Variation Archive Release 3, as generated by the UCSC Genome Browser (Supplementary Fig. 5). The finding of enriched nucleotide variants near the binding sites of BRD9 at *Stat1*, further enlightens that the critical epigenetic regulation of BRD9 relates to human disease.

Collectively, all these results demonstrate that BRD9 promotes *Stat1* transcription by directly regulating its promoter and enhancer activity.

FOXP1 interacts with BRD9 on *Stat1* transcriptional regulation

It is well-documented that chromatin remodeler regulates tissue- and stage-specific gene transcription with the facilitation of cofactors containing DNA sequence-specific binding functions[26,27]. As a critical component of the ncBAF complex, the biological roles of BRD9 largely depend on the collaborating TFs and the specific context[11,13,28]. To investigate the chromatin remodeling function of BRD9 and cofactors possibly facilitating the negative action of BRD9 on osteoclastogenesis, we conducted the Assay for Transposase-Accessible Chromatin with high throughput sequencing (ATAC-seq) and motif analysis.

The chromatin accessibility profile changed significantly with 12988 peaks in control group and 10795 peaks in BRD9 inhibition group, among which there are 6092 overlap peaks (Fig. 6a, b). Differentially accessible regions (DARs) between two groups were further compared and showed 3165 gain DARs and 2489 loss DARs after BRD9 inhibition ($|\log_2(\text{fold change})| > = 0.5$) (Fig. 6c). Then the gain and loss DARs around TSS after BRD9 inhibition were annotated and enriched using GO analysis (Fig. 6d). Significant GO terms enriched in gain DAR-genes after BRD9 inhibition related to the phosphatidylethanolamine, glycerolipid, and phospholipid biosynthetic process, which were reported to promote osteoclast fusion[29,30]. And significant GO terms enriched in loss DAR-genes after BRD9 inhibition related to apoptotic signaling and catecholamine/dopamine metabolic process, which were reported suppressing osteoclast differentiation[31]. The change on the chromatin accessibility landscape after BRD9 inhibition suggests, beside of IFN-β signaling pathway, multiple affected processes could also contribute to BRD9-mediated negative regulation on osteoclastogenesis.

To identify potential interacting TFs of BRD9 during osteoclastogenesis, the top enriched loss motifs after BRD9 inhibition using the ATAC-seq data (Fig. 6e), were compared with BRD9 binding sites enriched motifs using the ChIP-seq data. Motifs enriched in BRD9 binding sites while loss after BRD9 inhibition suggests their potential cooperative interaction with BRD9, such as MXI1, SRY, Arid3a, ZNF354C, FOXP1 (Fig. 6f).

Among these motifs, we noticed FOXP1 (Fig. 6g), a member of the hepatic nuclear factor-3/forkhead domain family of winged-helix transcription factors, that is indispensable for normal development

events[32]. Previous study has shown that overexpressing human *FOXP1* in monocyte/macrophage lineage cells using the CD68 promoter attenuated osteoclastogenesis and bone resorption activity in transgenic mice, suggesting the negative regulatory function of FOXP1 on osteoclast differentiation[33]. While the cellular mechanism and downstream signaling pathways is still unclear. We found that FOXP1 is expressed in CTSK + osteoclasts underneath the growth plate in the distal femur and osteoclasts (Fig. 6h, i). Based on the finding of its co-occupancy with BRD9 at genome above, we further hypothesized that FOXP1 may participate in the inhibitory function of BRD9 during osteoclastogenesis, at least partially through STAT1/IFN-β signaling pathway.

We scanned that FOXP1 TF-binding-site motif hits in the transcriptional regulatory region of *Stat1* and found there are multiple hits in the predicted proximal promoter region and enhancer region, where BRD9 binding (Supplementary Fig. 6). Then, co-immunoprecipitation (IP) assay confirmed the physical interaction between BRD9 and FOXP1 in BMDMs during osteoclast differentiation (Fig. 6j). To further validate the binding and transcriptional regulation function of FOXP1 on *Stat1*, we conducted ChIP-qPCR and *Foxp1* knockdown assay using lentivirus vector. As expected, we validated FOXP1 could bind to the *Stat1* promoter and enhancer directly, where BRD9 binding, while the binding function of FOXP1 at *Stat1* was compromised after BRD9 inhibition (Fig. 6k). And *Foxp1* knockdown with lentivirus vector leads to downregulated *Stat1*, accompanied with upregulation of osteoclastic differentiation genes compared with control lentivirus group, recapturing the regulatory function of BRD9 (Fig. 6l). We further excluded the possibility that it is the downregulated gene expression of *Foxp1* after BRD9 deletion or inhibition that leads to the compromised binding and regulatory function at *Stat1*, as shown with unchanged gene expression of *Foxp1* in BMDMs from *LysM-Cre;Brd9^fl/fl^* mice compared with that from control littermates after RANKL-induction (Fig. 6m) and in BMDMs from wild-type mice after BRD9 inhibition (Fig. 6n).

In summary, these results clearly show that FOXP1 is one of the critical cofactors of BRD9 during *Stat1* transcriptional activation and their negative feedback regulation during osteoclastic differentiation (Fig. 6o).

Function specificity of BRD9 distinguished from BRD4

PROTACs (Proteolysis-Targeting Chimeras), the direct protein-specific degradation using bifunctional molecules with peptides to bridge E3 ligases and target protein ligand, are reported as a promising therapeutic strategy for various diseases in clinical trials[34]. We have further evaluated the function of BRD9 during osteoclastogenesis using a chemical PROTAC BRD9 degrader, dBRD9[35]. Consistently, we confirmed the dose-dependent increase on the number and size of TRAP + multinuclear differentiated osteoclasts from RANKL-induced BMDMs with dBRD9 treatment, without apparent cell toxicity under the concentration of 1 μM (Fig. 7a, b). The concentration of 0.3 μM dBRD9 was chosen for further evaluations for its most prominent function on promoting osteoclastogenesis. Consistent with the results using iBRD9, we identified IFN-β signaling activity, as one of the top
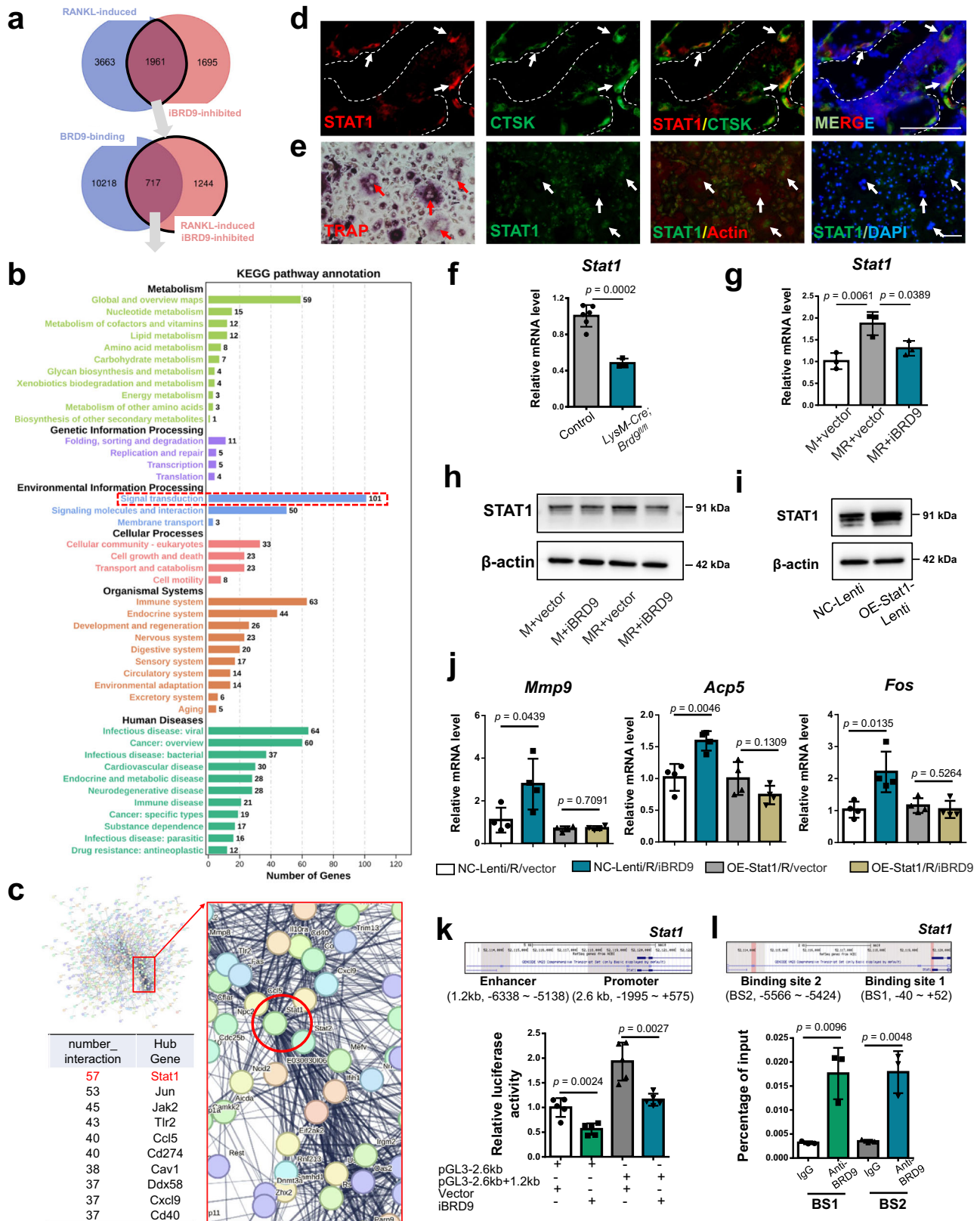
downrequlated signaling pathways after BRD9 degradation based on the transcriptional profile (Supplementary Table 1) and found that BRD9 degradation leads to enhanced expression of osteoclastogenic genes of *Mmp9*, *Acp5*, *Dcsstamp*, and downregulated expression of *Stat1* (Fig. 7c). Furthermore, the increased osteoclastogenesis after dBRD9 treatment was rescued after IFN-β signaling upregulation, as shown with the decreased number and size of TRAP + differentiated

osteoclasts (Fig. 7d), as well as the downregulated expression of osteoclastogenic genes of *Mmp9*, *Acp5*, and *Dcstamp* (Fig. 7e).

It is reported that BRD9 regulates macrophage activation via cooperation with BRD4[12]. In contrast to our findings of the inhibition function of BRD9 on osteoclastogenesis, previous studies showed BRD4 inhibition suppressed RANKL-induced osteoclastogenesis[22]. To distinguish the function specificity of BRD9 with BRD4, we have

Fig. 5 | STAT1 is critical for BRD9-mediated negative feedback during osteoclastogenesis. a Venn diagram showing overlapping genes, where BRD9 binding, RANKL-induced while downregulated after BRD9 inhibition. **b** KEGG pathway annotation of the genes, where BRD9 binding, RANKL-induced while downregulated after BRD9 inhibition. **c** Protein-protein interaction (PPI) networks of the genes, where BRD9 binding, RANKL-induced while downregulated after BRD9 inhibition. **d** Immunofluorescence staining of STAT1 (red) and CTSK (green) in the mouse distal femur at 4 weeks of age. Scale bar,100 μm. **e** Immunofluorescence of STAT1 (green), TRAP staining (red) and actin (red) in BMDMs after 3 days of RANKL-induction. Scale bar, 100 μm. **f** The mRNA expression of *Stat1* in BMDMs from *LysM-Cre;Brd9$^{fl/fl}$* mice compared with that from control littermates after 3 days of RANKL-induction. *n* = 3 for *LysM-Cre;Brd9$^{fl/fl}$* mice group. *n* = 6 for control littermates. **g** The mRNA expression of *Stat1* in BMDMs treated with iBRD9 after 2 days of RANKL-induction. *n* = 3 biologically independent samples. **h** The protein expression of STAT1 in BMDMs treated with iBRD9 after 2 days of RANKL-induction. **i** The protein expression of STAT1 in RAW264.7 transfected with control lentivirus (NC) and *Stat1*-overexpression lentivirus (OE-Stat1). **j** The mRNA expression of *Mmp9*, *Acp5* and *Fos* in *Stat1*-overexpressed and control RAW264.7 treated with iBRD9 after 2 days of RANKL-induction. *n* = 4 biologically independent samples. **k** Luciferase reporter activities of the *Stat1* promoter alone or in the presence of enhancer region in osteoclastic induced RAW264.7 treated with iBRD9 or control vector. *n* = 5 biologically independent samples. **l** ChIP assay with BRD9 antibody (or IgG) in RAW264.7 cell line during osteoclastic induction. *n* = 3 biologically independent samples. All data in this figure are represented as mean ± SD. Two-tailed Student's *t*-test for (**f**), (**j**), (**k**), and (**l**). One-way analysis of variance (ANOVA) with Tukey's multiple comparisons test for (**g**). M, M-CSF; MR, M-CSF + RANKL. All experiments were performed in triplicates unless otherwise stated. Source data are provided in the Source data file.

compared the transcriptional profile after BRD9 degradation with dBRD9 and BRD4 inhibition with JQ1 during osteoclastogenesis. Besides of the apparent opposite change on the osteoclast-related genes (Fig. 7f), the enriched top ten changed signaling pathway in JQ1-treated group compared with the dBRD9-treated group were listed (Fig. 7g). We have noticed that the cell cycle and osteoclast differentiation process are on the top changed pathways in JQ1-treated group compared with dBRD9-treated group. The cell cycle-related signature genes were apparent downregulated in JQ1-treated group (Fig. 7h), suggesting their potential roles leading to the opposite effect between dBRD9 and JQ1 during osteoclastogenesis. The solid mechanism studies need to be fulfilled in the further.

BRD9 degrader mitigates ZOL-related ONJ
ZOL-related ONJ is related to compromised osteoclastogenesis in patients after tooth extraction, with long-term medication of strong anti-bone resorptive agents[36]. In addition, recent studies have also unveiled that the pathogenesis of ONJ is also related to excessive macrophage activation and inflammation process[37]. While, no clinical procedure is available to prevent or effectively treat ONJ at present. Given the efficacy of chemical PROTAC dBRD9 shown in preclinical models of synovial sarcoma and leukemias[10,38], we presumed that local treatment of dBRD9 degrader that characterized with both pro-osteoclastogenesis and anti-inflammatory response[12,13], could prevent or mitigate ONJ effectively.

To test this hypothesis, we sought to develop a mouse model of ONJ-like disease by treating 6-week-old WT C57BL/6J mice with ZOL (125 μg/kg body weight; twice per week) and DEX (5 mg/kg body weight; weekly) for 4 weeks[39]. Two weeks after the initial ZOL/DEX injection, the maxillary left first molar was extracted from the mice. Silk fibroin (SF) has been widely used in bone tissue engineering due to its biocompatibility and controlled biodegradability[40]. In addition to providing suitable platforms for diverse chemical cues, the injectable and photocuring properties of SF entitled it as an ideal biomaterial for the bone regeneration of tooth extraction sockets in oral medicine. Therefore, a modified injectable photocuring SF containing BRD9 degrader was constructed and filled into the alveolar bone sockets immediately after tooth extraction, with SF containing vector as control group. After another two weeks, the maxillary bones in each group were collected for evaluation (Fig. 8a).

Alveolar bone healing assessment by μCT imaging showed severe periosteal reaction (Fig. 8b, arrow 1), hyper-osseous maxillary sinus floor (Fig. 8b, arrow 2) and insufficient amount of bone filled with osteosclerotic patterns and sequestrum (Fig. 8b, arrow 3) at the molar extraction site in the mice from ONJ-control vector group. While the molar extraction sockets in the mice from ONJ-dBRD9 group are filled with well-organized newly formed trabecular bone (Fig. 8b), with 80% reduced incidence rate of osteonecrosis and periosteal reaction compared within the mice from ONJ-control vector group (Fig. 8c).

Histologic examination showed that the necrotic alveolar bone with empty lacunae in control mice (Fig. 8d, asterisk) were much attenuated in the healed extraction sockets in the dBRD9 group with well-organized bone tissue structure infilled with blood vessels (Fig. 8d, arrowhead).

TRAP staining and quantification analysis showed the locally increased osteoclasts that participating the active bone remodeling on the bone surface of the healed extraction sockets in dBRD9 degrader treated group comparing with the control group (Fig. 8e, f). Immunofluorescence staining of iNOS (Fig. 8g), TNF-α (Fig. 8h) and CD86 (Fig. 8i) showed the locally alleviated inflammatory response on the bone surface of the healed extraction sockets in dBRD9 degrader treated group comparing with the control group.
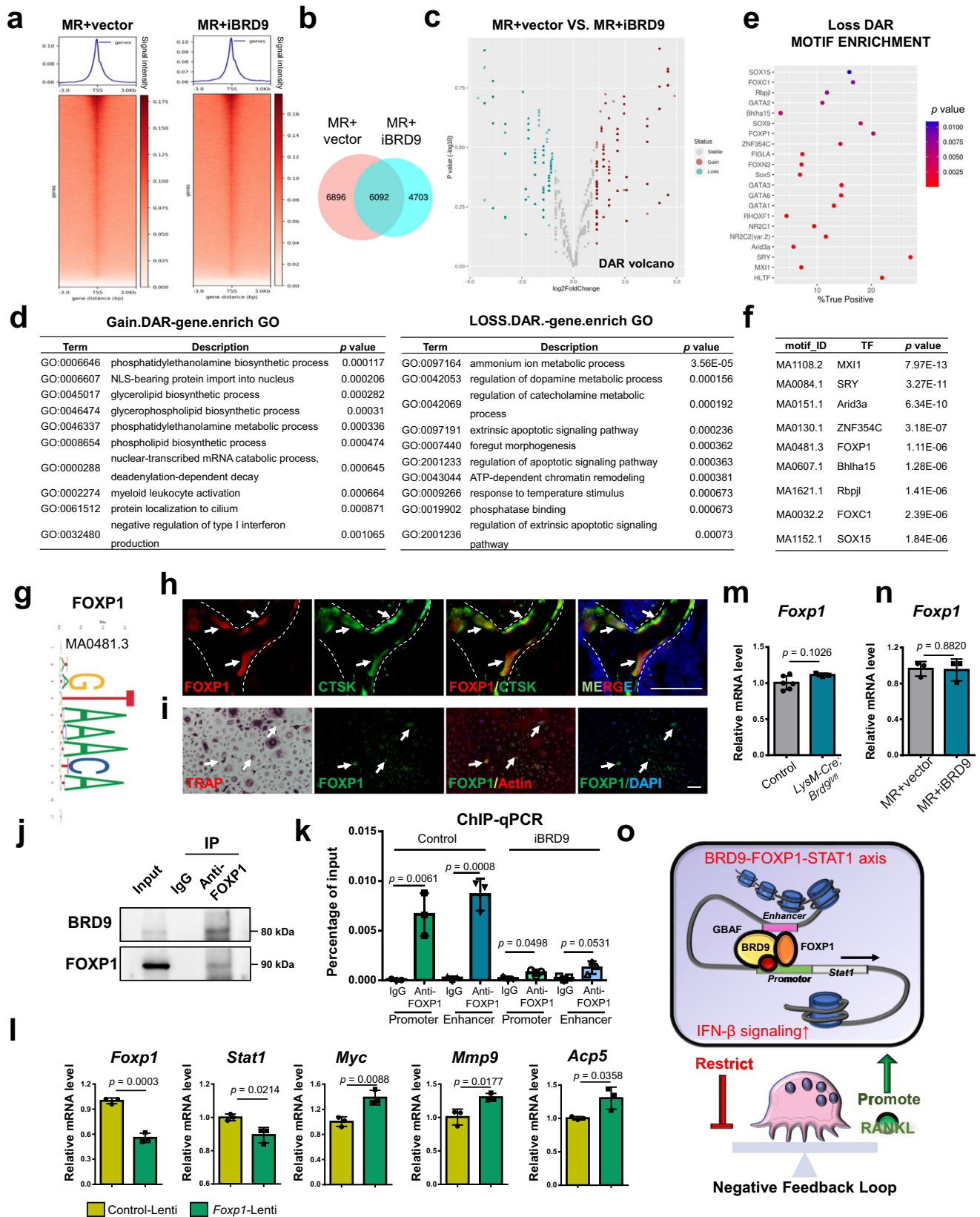
The well-matched indications of applying dBRD9 for ZOL-induced ONJ urger us to investigate the potential linkage between the pathogenesis and BRD9 function during both osteoclastogenesis and macrophage activation. Interestingly, our preliminary data showed that ZOL treatment could lead to upregulated expression of BRD9 in BMDMs during both RANKL-induced osteoclastogenesis and lipopolysaccharide (LPS)-induced macrophage activation (Fig. 8j). The finding recalls the function mechanism of BRD9, and also suggests the application of dBRD9 for ZOL-induced ONJ is one potential ideal etiotropic therapy. As expected, as one of the critical downstream targets of BRD9, STAT1 is downregulated in dBRD9 degrader treated group comparing with the control group in vivo (Fig. 8k).

Taken together, leveraging the advantages of pharmacological modulation of BRD9 and flexible injectable SF biomaterial scaffolds, we designed a local bone regeneration system for tooth extraction defects, which effectively prevents and mitigates ZOL-related ONJ. These results echo the molecular mechanism of BRD9 proved in our study, and more importantly provide a promising therapeutic strategy to prevent or effectively alleviate ONJ for patients with a long-term ZOL medication history in the future.

BRD9 deletion/degradation mitigates LPS-induced bone resorption
It is well-documented that inflammatory stimuli usually upregulate RANKL expression in various types of cells such as bone marrow stromal cells and osteoblasts, and promote bone resorption, leading to overt bone loss in patients at clinical and animal models[41]. Given the inhibition role of BRD9 on anti-inflammatory response[12,13], it is necessary to figure out the change on inflammation response and RANKL expression, besides of osteoclastogenesis, in the bone tissue of the BRD9-depleted mouse under both unstimulated and stimulated condition.

The results showed that, without additional infection, loss of *Brd9* led to slight inhibition on the basal expression of proinflammatory cytokines, such as TNF-α, iNOS, CD86, IL-1b with no apparent effect on RANKL in the femur bone tissue as shown with immunofluorescence staining, as well as the quantification analysis using qPCR

d

Gain.DAR-gene.enrich GO

Term	Description	p value
GO:0006646	phosphatidylethanolamine biosynthetic process	0.000117
GO:0006607	NLS-bearing protein import into nucleus	0.000206
GO:0045017	glycerolipid biosynthetic process	0.000282
GO:0046474	glycerophospholipid biosynthetic process	0.00031
GO:0046337	phosphatidylethanolamine metabolic process	0.000336
GO:0008654	phospholipid biosynthetic process	0.000474
GO:0000288	nuclear-transcribed mRNA catabolic process, deadenylation-dependent decay	0.000645
GO:0002274	myeloid leukocyte activation	0.000664
GO:0061512	protein localization to cilium	0.000871
GO:0032480	negative regulation of type I interferon production	0.001065

LOSS.DAR.-gene.enrich GO

Term	Description	p value
GO:0097164	ammonium ion metabolic process	3.56E-05
GO:0042053	regulation of dopamine metabolic process	0.000156
GO:0042069	regulation of catecholamine metabolic process	0.000192
GO:0097191	extrinsic apoptotic signaling pathway	0.000236
GO:0007440	foregut morphogenesis	0.000362
GO:2001233	regulation of apoptotic signaling pathway	0.000363
GO:0043044	ATP-dependent chromatin remodeling	0.000381
GO:0009266	response to temperature stimulus	0.000673
GO:0019902	phosphatase binding	0.000673
GO:2001236	regulation of extrinsic apoptotic signaling pathway	0.00073

f

motif_ID	TF	p value
MA1108.2	MXI1	7.97E-13
MA0084.1	SRY	3.27E-11
MA0151.1	Arid3a	6.34E-10
MA0130.1	ZNF354C	3.18E-07
MA0481.3	FOXP1	1.11E-06
MA0607.1	Bhlha15	1.28E-06
MA1621.1	Rbpjl	1.41E-06
MA0032.2	FOXC1	2.39E-06
MA1152.1	SOX15	1.84E-06

(Supplementary Fig. 7). Localized aggressive periodontitis (LAP) is a common disease in oral medicine, which is characterized with hyperinflammatory response and acute severe bone loss. Therefore, LPS-induced in periodontal alveolar bone loss was used as a model to evaluated the change on inflammation response and RANKL expression, besides of osteoclast activity, in the bone tissue of the *Brd9*-depleted mouse (Fig. 9a). Interestingly, although carrying osteoporosis phenotype (Fig. 9b, c, asterisks), the *Brd9*-depleted mouse showed resistant to LPS/ligation-stimulated local acute damage on the periodontal alveolar bone (Fig. 9b–d) and osteoclast activity (Fig. 9e, f) compared with the control mice. Cellular and molecular examination results suggested the alleviated acute local bone loss and osteoclast

Fig. 6 | FOXP1 interacts with BRD9 to regulate *Stat1* transcription during osteoclastogenesis. a Heatmap showing the average ATAC-Seq signal centered on the transcription start site (TSS) of the nearest genes in osteoclastic induced BMDMs after control and iBRD9 treatment. Color scale represents average signal intensity. **b** Venn diagram showing the overlapping and discrepant peaks between control and iBRD9 group. **c** Volcano plot depicting differentially accessible region (DAR) between control and iBRD9 group. **d** GO terms of genes with gain and loss DAR around TSS after BRD9 inhibition. **e** Dot bubble plot showing the loss DAR motif enrichment after BRD9 inhibition. **f** Motifs enriched in BRD9 binding while loss after BRD9 inhibition. **g** The FOXP1 motif logo. **h** FOXP1 immunofluorescence (red) and CTSK (green) in the mouse distal femur at 4 weeks. Scale bar, 100 μm. **i** FOXP1 immunofluorescence (green), TRAP staining (red) and actin (red) in BMDMs after 3 days of RANKL-induction. Scale bar, 100 μm. **j** Co-IP assay with FOXP1 antibody (or IgG) in BMDMs during osteoclastic induction, followed by immunoblotting of BRD9 and FOXP1. **k** ChIP assay with FOXP1 antibody (or IgG) in RAW264.7 cell during RANKL-induction treated with iBRD9 or vector. *n* = 3 biologically independent samples. **l** The mRNA of *Foxp1*, *Stat1*, *Myc*, *Mmp9* and *Acp5* in osteoclastic induced RAW264.7 cell treated with *Foxp1* knockdown lentivirus (*Foxp1*-Lenti) or control lentivirus (Control-Lenti). *n* = 3 biologically independent samples. **m** The mRNA of *Foxp1* in BMDMs from *LysM-Cre;Brd9^{fl/fl}* (*n* = 3) and control mice (*n* = 6) at 4 weeks after 3 days of osteoclast differentiation. **n** The mRNA of *Foxp1* in BMDMs treated with iBRD9 after 3 days of osteoclast differentiation. *n* = 3 biologically independent samples. **o** Schematic drawing shows chromatin remodeling mediated by BRD9. All data in this figure are represented as mean ± SD. Negative binomial distribution used for **c**. Hypergeometric distribution test for **d**. the one-tailed Fisher's Exact test for (**e**) and (**f**). Two-tailed Student's *t*-test for (**m**), (**n**), (**k**), and (**l**). MR, M-CSF + RANKL. All experiments were performed in triplicates unless otherwise stated. Source data are provided in the Source data file.

activity might be benefit from the resistance to LPS/ligation-stimulated hyper-inflammatory response and increased RNAKL in *LysM-Cre;Brd9^{fl/fl}* mice compared with control mice, as shown with immunofluorescence staining of TNF-α, iNOS, and RANKL (Fig. 9g).

Inspired by above findings, to test the prevention and therapeutic potential of dBRD9 for LPS/ligation-induced acute periodontitis and alveolar bone loss, the modified injectable photocuring SF containing BRD9 degrader, was further utilized and injected into the periodontal tissue during LPS/ligation induction, with SF containing vector in the contralateral (Fig. 9h). After 5 days, the alveolar bones in each group were collected for evaluation. The results showed that LPS/ligation-stimulated acute local bone loss (Fig. 9i–k), osteoclast activity (Fig. 9l, m), as well as macrophages activation and RANKL expression (Fig. 9n, o) in the periodontal alveolar bone were much attenuated in the dBRD9 group compared with control vector group.

Taken together, the anti-inflammatory effect of BRD9 deletion or degradation in bone tissue is likely more prominent under infection stimulated circumstance compared within the basal condition.
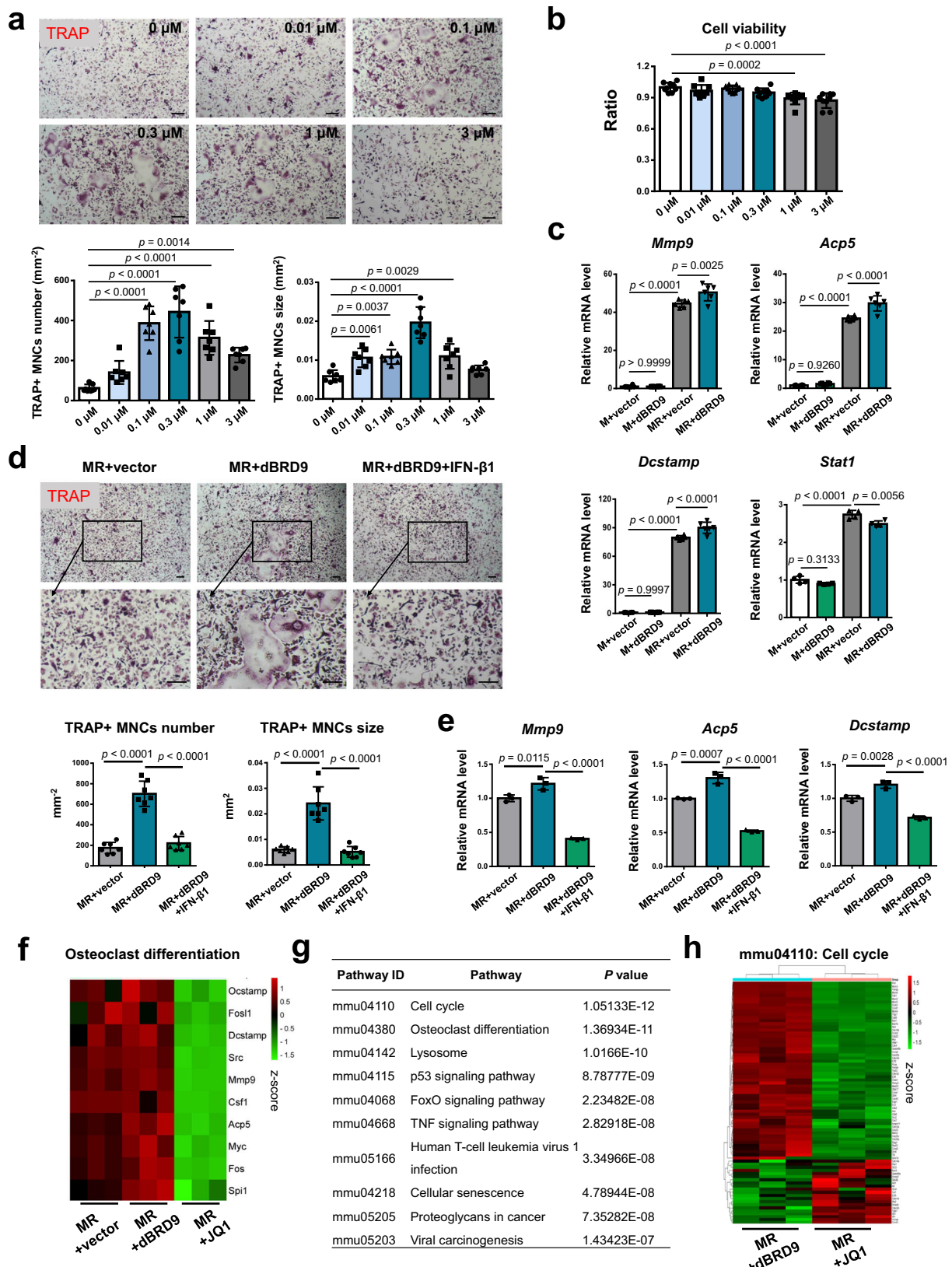
Discussion

With the deepening understanding on the epigenetics during key developmental processes in organogenesis, an increasing number of studies have defined epigenetic changes as determinants of gene expression in osteoclastogenesis[42–44]. For example, the demethylation of H3K27me3 in the *Nfatc1* gene locus by Jumonji domain-containing 3 plays a critical role in osteoclast differentiation[42]; KDM4B-CCAR1-MED1 signaling axis induces euchromatinization changes near the promoters of osteoclast-related genes through H3K9 demethylation[44]. While the relationship between chromatin remodeler and osteoclast differentiation remains incompletely defined. Recent studies revealed that BRD9-mediated chromatin remodeling cooperates with TFs to modulate the expression of lineage-specific or stimulus-induced genes in cancer cell proliferation[45], pluripotency[9], inflammatory responses[12,13,15] and antiviral activity[46,47]. For example, in mouse embryonic stem cells, BRD9 targets distinct genomic features from those targeted by canonical BAF complex and maintains members of the transcriptional network associated with pluripotency[9]; in cytokine stressed β-cells, inhibition of BRD9 increases the anti-inflammatory function of vitamin D receptor (VDR) through modulating VDR and BRD9 interaction to limit β-cell failure[15]; in macrophages, BRD9 acts as a genomic antagonist of glucocorticoid receptor (GR) at inflammatory-related genes, restricting the therapeutic efficacies of glucocorticoids on repressing inflammatory responses[13]. While the role of BRD9 in osteoclast formation is only now being addressed in our study. We revealed that BRD9 interacts with FOXP1 and provides chromatin accessibility for it at *Stat1* promoter and enhancer, activating IFN-β signaling thereafter. The finding of transcriptional activator role of BRD9 echoes the result from previous study that BRD9-binding sites are mainly associated with active chromatin regions in genome[7], and also highlights the context-dependent roles of BRD9-containing ncBAF complex and its diverse cofactors in maintaining transcriptional networks in physiological and pathological process. Nevertheless, BRD9 is a rather conserved positive regulator of the Type I interferon signaling pathway and interferon-stimulated genes in multiple cell types whether that function is inflammatory[12,13], antiviral[46,47], or negative feedback as in the case of osteoclastogenesis in our study.

Previous mass spectrometry-based interaction proteomics experiments identified bromodomain as a major acetyl-lysine readers, associating with regulatory active enhancers[15,48]. IBRD9 is BRD9 bromodomain inhibitor and functions via impairing the acetyl-lysine recognition of BRD9[14]. Besides of proximal promoter, we observed enhancer-associated transcriptional abnormalities at *Stat1* in RAW264.7 cells after BRD9 inhibition, indicating that the regulatory role of BRD9-containing ncBAF, at least in part, via bromodomain-mediated interactions with chromatin regions marked with acetyl-lysine modifications.

Similar with BRD9, the bromodomain and BET protein family (BRD2, BRD3, BRD4, and BRDT) is also an important subfamily of bromodomain protein superfamily[49]. Interestingly, previous work demonstrated that a pan-BET protein inhibitor I-BET151 or a typical class of BRD4 inhibitors JQ1, suppressed osteoclast formation with inhibition on TRAP, MMP-9, and CTSK, by blocking RANKL-mediated MYC-NFAT axis, MAPK, and NF-κB pathways[50–53]. Therefore, although a recent study declaims that BRD9 regulates macrophage activation via cooperation with BRD4[12], it is not likely the same case as for osteoclastogenesis. Our preliminary data showed the downregulated genes in JQ1-treated group compared with dBRD9-treated group, are enriched on cell cycle, ribosome biogenesis and DNA replication. Actually, BRD4 is reported conducting critical and general role in transcription regulation, in the genome of various normal and transformed cell types[54,55]. As such, *Myc*, which is essential for both cell cycle in tumorigenesis and TF regulatory network in osteoclastogenesis, is one conserved target of BRD4[22,52,56]. Therefore, BRD4-mediated transcription activation of genes, such as *Myc*, could entitle BRD4 the tumorigenic role and also positive role in osteoclastogenesis, which is distinct with the function of BRD9 demonstrated in our study. Solid mechanism studies with high-resolution insights into these transcriptional regulation processes mediated by these distinct factors needs to be explored in further studies.

FOXP1 contains both DNA-binding- and protein-protein binding-domains. It is reported that FOXP1-mediated repression of Jagged1 is pivotal in regulating embryonic neural stem cells differentiation[57]; FOXP1 binds to CSF1R promoter with corepressor NCOR2 involving in regulation of monocyte differentiation and macrophage functions[33]; and FOXP1 physically interacts with silencing mediator for retinoid and thyroid receptor and recruited to the *p21* promoter during myocardial development[58]. In bone tissue, it is also demonstrated that FOXP1 transcriptionally controls senescence and fate commitment of BMSCs via directly represses transcription of p16INK4A at promoter region or repress adipogenesis and osteogenesis-associated genes through

a TRAP

b Cell viability

c *Mmp9* *Acp5* *Dcstamp* *Stat1*

d MR+vector · MR+dBRD9 · MR+dBRD9+IFN-β1 · TRAP

e *Mmp9* *Acp5* *Dcstamp*

f Osteoclast differentiation

g

Pathway ID	Pathway	P value
mmu04110	Cell cycle	1.05133E-12
mmu04380	Osteoclast differentiation	1.36934E-11
mmu04142	Lysosome	1.0166E-10
mmu04115	p53 signaling pathway	8.78777E-09
mmu04068	FoxO signaling pathway	2.23482E-08
mmu04668	TNF signaling pathway	2.82918E-08
mmu05166	Human T-cell leukemia virus 1 infection	3.34966E-08
mmu04218	Cellular senescence	4.78944E-08
mmu05205	Proteoglycans in cancer	7.35282E-08
mmu05203	Viral carcinogenesis	1.43423E-07

h mmu04110: Cell cycle

interactions with the CEBPβ/δ complex or RBPjκ, respectively[59]. Contrary to its well-known repressor or corepressor role during organogenesis, our study has presented that FOXP1 binds to previously uncharacterized sites within the proximal promoter and enhancer of *Stat1*, functioning as a transcriptional co-activator with BRD9. This finding of the cooperation between FOXP1 and chromatin remodeler BRD9 not only expands its pleiotropic gene regulatory function, but also further highlights its cell type-specific manner during organogenesis.

Beside of FOXP1, other TFs could also cooperate with BRD9 during the negative feedback regulation during osteoclastogenesis. For example, it is reported that MXI1 (Max interactor 1), interacts

Fig. 7 | Function specificity of BRD9 distinguished from BRD4. a TRAP staining and quantification analysis of RANKL-induced BMDMs with 3 days of dBRD9 at different concentration. Scale bar, 200 μm. *n* = 7 biologically independent samples. **b** Cell viability of RANKL-induced BMDMs with 1 day of dBRD9 at different concentration, shown by cell counting kit 8 assay. *n* = 9 biologically independent samples. **c** The mRNA expression of *Mmp9, Acp5, Dcstamp,* and *Stat1* in BMDMs after 2 days of 0.3 μM dBRD9 or vector treatment with or without RANKL-induction, as measured by qPCR. *n* = 6 biologically independent samples for *Mmp9, Acp5, Dcstamp; n* = 4 biologically independent samples for *Stat1*. M-CSF, M; RANKL, R. **d** TRAP staining and quantification analysis of BMDMs treated with 3 days of 0.3 μM dBRD9 and 0.0625 ng/ml IFN-β1 during osteoclastic induction. Scale bar, 200 μm. *n* = 7 biologically independent samples. **e** The mRNA expression of *Mmp9, Acp5* and *Dcstamp* in BMDMs treated with 2 days of 0.3 μM dBRD9 and 0.0625 ng/ml IFN-β1

during osteoclastic induction, as measured by qPCR. *n* = 3 biologically independent samples. M-CSF, M; RANKL, R. **f** Heatmap showing the change on the transcriptional profile of critical osteoclast-related genes between dBRD9 and JQ1 treated BMDMs during osteoclastogenesis. **g** GO analysis shows the enriched top ten changed signaling pathway in JQ1-treated group compared with the dBRD9-treated group. **h** Heatmap showing the cell cycle-related signature genes in JQ1-treated group compared with the dBRD9-treated group during osteoclastogenesis. All data in this figure are represented as mean ± SD. Hypergeometric distribution test for **g**. One-way analysis of variance (ANOVA) with Dunnett's multiple comparisons test for (**a**) and (**b**); with Tukey's multiple comparisons test for (**c**), (**d**), and (**e**). Color scale in **f** and **h** represents normalized gene FPKM value by z-score scheme. All experiments were performed in triplicates unless otherwise stated. Source data are provided in the Source data file.

specifically with Max to form heterodimers antagonizing the transcription activation of MYC[60]. Although there is lack of direct function evidence, the critical role of MYC in osteoclast differentiation implicates the potential repressor role of MXI1 during osteoclastogenesis. In addition, the decreased SRY (sex-determining region Y) is reported to related with the increased incidence of osteoporosis in human bone samples[61]. The potential cooperative interaction of BRD9 with these enriched TFs, further emphasized the critical role of BRD9-mediated chromatin remodeling during the negative regulation on osteoclastogenesis.

In this study, we confirmed the synergizing function of BRD9 inhibition and glucocorticoids during osteoclastogenesis, and the functional categories of iBRD9/DEX cooperatively regulated genes were enriched on metabolic process during osteoclastogenesis. Although it is distinct with iBRD9-alone regulated gene network, we still could get inspires from Wang et al.'s study[13]. The authors found that during macrophage activation, BRD9 loss could affect the glucocorticoid response of a set of GR binding sites that associated with cell metabolism and cell–cell adhesion, although without significant colocalization of BRD9, while through redistributing their GR binding to the sites associated with the inflammatory response gene network. While the underling sophisticated interaction and regulation network needs to be explored in further studies.

Our preliminary data showed that ZOL treatment leads to upregulated expression of BRD9 in BMDMs during both osteoclastogenesis and macrophage activation. The finding recalls the function of BRD9 on restricting osteoclastogenesis and promoting inflammatory response[12,13], and also suggests the application of dBRD9 for ZOL-induced ONJ is one ideal etiotropic therapy. It provides clues extending our understanding on bisphosphonates mechanism of action and is worth further investigation. In addition, we also find that the acute bone loss caused by LPS-induced hyper-inflammatory response is kind of exempted from BRD9 deletion/degrader during the pathogenesis. Therefore, the complex osteoimmunology underlying the function of BRD9 on osteoclastogenesis and inflammatory response in physiological and pathological condition, is remained to be investigated deeply.

In summary, our study has identified a BRD9-FOXP1-STAT1 axis that is indispensable for the negative feedback loop and homeostasis of osteoclasts. These findings further expand our knowledge of the delicate interaction network among chromatin remodelers, TFs, and signaling pathways the homeostasis of bone-immune circuit, and also shed light on developing attractive therapeutic strategies for osteoclast-associated bone disease in the future.

Methods
Mice
Brd9-flox mice (Strain NO. T008489), *LysM-Cre* mice (Strain NO. T003822), and WT C57BL/6J mice (Strain NO. N000013) from Gem-Pharmatech (Nanjing, China) and tdTomato (Strain NO. 007909) mouse line[62] from Jackson Laboratory (Maine, USA) were used and cross-bred in this study. All mice were used for analysis regardless of

sex. All mice were housed in pathogen-free conditions with constant ambient temperature (22 ± 2 °C) and humidity (55 ± 10%), with an alternating 12-h light/dark cycle. All mice were euthanized by carbon dioxide overdose followed by cervical dislocation. All animal studies were approved by the Institutional Animal Care and Use Committee at Ninth People's Hospital, School of Medicine, Shanghai Jiao Tong University (SH9H-2022-A926-1).

ZOL-related ONJ model
Six-week-old WT C57BL/6J mice were subjected to an injection of 125 μg/kg body weight ZOL (446, S1314, Selleck) intraperitoneally twice a week and 5 mg/kg body weight DEX (Sigma-Aldrich, D-085) subcutaneously weekly for 4 weeks (*n* = 5 per group). Under general anesthesia, the left maxillary first molar was atraumatically extracted 2 weeks after the initial injection. Silk fibroin protein was extracted from Bombyx mori cocoons[40]. Briefly, de-sericin process was performed by boiling Bombyx mori cocoons in Na$_2$CO$_3$ solution. After dissolved and dialyzed, the regenerated silk solution (3% w/v) was further frozen before lyophilization. To improve its stability in aqueous environments, scaffolds were autoclaved to induce β-sheet formation. Then dBRD9 (R&D, 6606) was mixed within the silk fibroin hydrogel at the final concentration of 0.3 mM before injection. Two weeks after the tooth extraction, the mice were sacrificed to harvest the maxilla from each mouse for μCT imaging, histologic and molecular examination.

LPS/ligation induced periodontal bone loss model
To evaluate LPS-induced in periodontal alveolar bone loss, the 5-0 silk sutures soaked in 2 mg/ml LPS (Sigma-Aldrich, L2880) were placed between the cervical of the first and second maxillary molars in control and *Brd9*-depleted mouse under general anesthesia at 4-week-old. One week after the LPS/ligature application, the mice were sacrificed to harvest the maxilla from each mouse and fixed. After μCT scanning, these tissues were decalcified before processed for histological analysis. To test the prevention and therapeutic potential of dBRD9 for LPS-induced alveolar bone loss, the modified injectable photocuring SF containing BRD9 degrader, mentioned above, was further utilized and injected into the periodontal tissue during LPS/ligation induction in six-week-old WT C57BL/6J mice, with SF containing vector in the contralateral. After 5 days, the alveolar bones in each group were collected for μCT imaging, histologic and molecular examination.

Micro-CT analysis
Micro-CT (μCT) analysis of fixed femur or maxillary bone was performed using a Skyscan 1176 (Bruker, Kontich, Belgium) at 50 kVp, 450 μA and a resolution of 9 μm. The obtained images were reconstructed with NRecon software (v1.7.1.0, Bruker, Kontich, Belgium). The region from 50 to 250 slices below the growth plate was analyzed for BV/TV, Tb.Th., Tb.N., and Tb.Sp, and the region from 500 to 550 slices below the growth plate was analyzed for Ct.Th and Ct.Pm using the program CTAn (v 1.16, Bruker, Kontich, Belgium).
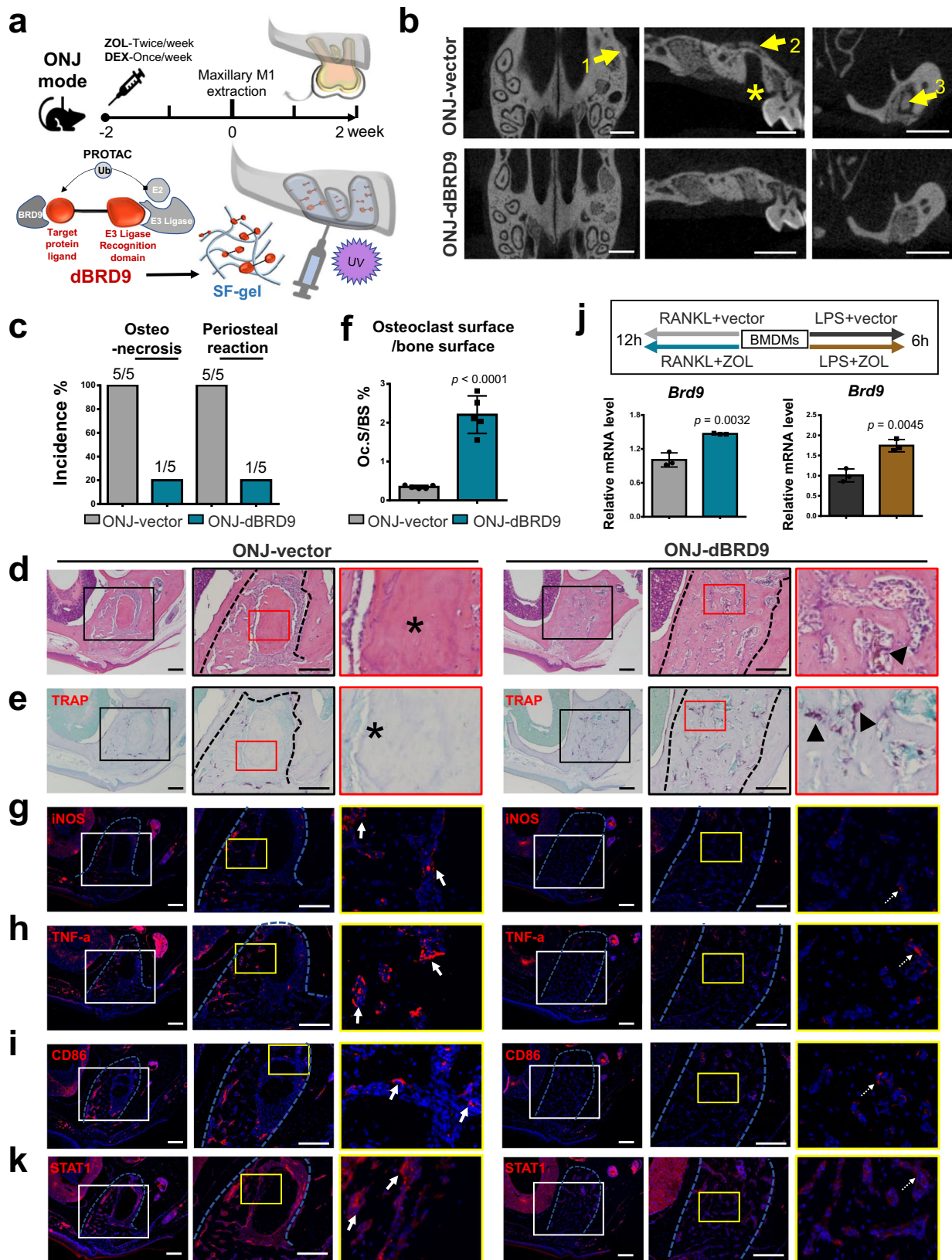
Histological analysis

Mouse femur or maxillary bone were dissected and fixed, followed by decalcification in 10% EDTA in PBS for 1–3 weeks depending on the age of the samples. The decalcified samples were dehydrated with serial ethanol and xylene and embedded in paraffin. The paraffin-embedded samples were then cut into sections with a thickness of 4 mm using a

microtome (Leica). H&E staining (servicebio, G1005), von kossa staining (servicebio, G1043), TRAP Staining (sigma, 387 A) and ALP staining (Beyotime, C3206) were conducted following the manufacturer's standard protocol. For dynamic bone histomorphometric analysis, double fluorescence labeling was performed[63]. Briefly, calcein (Sigma-Aldrich, C0875, 25 mg/kg) and Alizarin Red S (Sigma-Aldrich, A5533, 30 mg/kg)

Fig. 8 | BRD9 degrader mitigates ZOL-related ONJ after tooth extraction.
a Schematic illustrating the protocol used to establish ZOL-related ONJ model and
dBRD9 degrader treatment. **b** μCT imaging of the maxillary bone from mice in
dBRD9 degrader treated group and the control group. Yellow arrow 1 indicates
severe periosteal reaction. Yellow arrow 2 indicates hyper-osseous maxillary sinus
floor. Yellow arrow 3 indicates osteosclerotic patterns and sequestrum. Asterisk
indicates insufficient amount of bone. Scale bar, 1 mm. **c** The incidence rate of
osteonecrosis and periosteal reaction of the maxillary bone from mice in dBRD9
degrader treated group and the control group. $n = 5$. **d** H&E staining of the peri-
odontal and alveolar bone area from mice in BRD9 degrader treated group and the
control group. Colored boxes in the left are shown at higher magnification in right.
Black dashed lines outline the boundary of the healed extraction sockets. Asterisk
indicates necrotic alveolar bone with empty lacunae. Scale bar, 200 μm. **e** TRAP
staining and **f** quantification of the periodontal and alveolar bone area from mice in

BRD9 degrader treated group and the control group. Colored boxes in the left are
shown at higher magnification in right. Arrows point to TRAP-positive osteoclasts.
Asterisk indicates no signal. Scale bar, 200 μm. $n = 5$. Immunofluorescence staining
of **g** iNOS (red), **h** TNF-a (red), **i** CD86 (red), **k** STAT1 (red) of the periodontal and
alveolar bone area from mice in BRD9 degrader treated group and the control
group. Colored boxes in the left are shown at higher magnification in right. Blue
dashed lines outline the boundary of the healed extraction sockets. Arrows indi-
cates positive signal. Scale bar, 200 μm. **j** The mRNA expression of *Brd9* in ZOL or
vector-treated BMDMs during LPS-induced macrophage activation and RANKL-
induced osteoclastogenesis at indicated timepoint. $n = 3$ biologically independent
samples. All data in this figure are represented as mean ± SD. Two-tailed Student's *t*-
test for (**f**) and (**j**). All experiments were performed in triplicates unless otherwise
stated. Source data are provided in the Source data file.

---

were administered to mice by intraperitoneal injection at 7 d and 2 d
before sacrifice, respectively. Then the uncalcified bone tissues were
dehydrated and embedded before sectioned at 8 mm. Nikon Eclipse
Ti-U Microscope (Nikon, Japan) with NIS-Elements software
(v4.5000.1117.0) and Zeiss Axio Scope A1 Microscope (ZEISS, German)
with DP2-TWAIN software (v3.0.0.6212) were used to acquire images.

Immunofluorescence staining
The decalcified samples were dehydrated in serial sucrose solutions
and embedded in OCT compound (Tissue-Tek, Sakura). OCT-
embedded samples were cryosectioned at 8 mm using a cryostat
(Leica CM1850) followed by staining. For immunofluorescence stain-
ing, cryosections were soaked in blocking solution for one hour at
room temperature and then incubated with primary antibodies diluted
in blocking solution at 4 °C overnight. After washing three times in
PBS, the sections were incubated with alexa-conjugated secondary
antibodies and counterstained with DAPI. Antibodies used in immu-
nofluorescence staining as following: BRD9 antibody (Abcam,
ab259839, 1:100), CTSK antibody (Abcam, ab37259, 1:100), STAT1
antibody (Cell signaling, 9172, 1:100), FOXP1 antibody (Merck Milli-
pore, ABE68, 1:100), RUNX2 antibody (Thermo Fisher Scientific, MA5-
41185, 1:100), iNOS (Abcam, ab178945, 1:100) TNF-a (Thermo Fisher
Scientific, PA5-19810, 1:100), CD86 (Cell signaling, 19589, 1:100),
RANKL antibody (bioworlde, BS72037, 1:100), Goat anti-Rabbit IgG
(H + L) Cross-Adsorbed Secondary Antibody, Alexa Fluor 488 (Thermo
Fisher Scientific, A-11008, 1:200), Donkey anti-Rabbit IgG (H + L) Highly
Cross-Adsorbed Secondary Antibody, Alexa Fluor 594 (Thermo Fisher
Scientific, A-21207, 1:200), Goat anti-Mouse IgG (H + L) Cross-
Adsorbed Secondary Antibody, Alexa Fluor 488 (Thermo Fisher Sci-
entific, A-11001, 1:200) and Goat anti-Mouse IgG (H + L) Cross-
Adsorbed Secondary Antibody, Alexa Fluor 594 (Thermo Fisher Sci-
entific, A-11005, 1:200).

Cell culture
Bone marrow cells were harvested from murine femurs of four to six-
week-old WT C57BL/6J mice and cultured in α-minimum essential
medium (α-MEM) containing 10% FBS and 1% penicillin-streptomycin
overnight (Thermo Fisher Scientific, Waltham, MA, USA). For osteo-
clast induction, BMDMs were cultured into complete media with
50 ng/ml recombinant soluble murine M-CSF (PeproTech, 315-02) and
100 ng/ml recombinant soluble murine RANKL (PeproTech, 315-11).
For activation of macrophages, BMDMs were cultured into complete
media supplemented with 100 ng/ml LPS. RAW264.7 cells (Cyagen
Biosciences, M3-0101) were maintained in DMEM media containing
10% FBS, 1% penicillin/streptomycin[63]. For osteoclast induction,
RAW264.7 cell were cultured in presence of 100 ng/ml RANKL.
   For the BRD9 inhibitor/degrader experiments, the cells were
treated with either vehicle or varying concentrations of iBRD9 (Tocris
Bioscience, 5591) or dBRD9 (R&D Systems, 6606) twenty-four hours
after plated, as well as IFN-β1 cytokine (0.0625 ng/ml, R&D Systems,

8234-MB), DEX (10^{-11}–10^{-9} M), JQ1 (0.25 μM, Abmole Bioscience,
M2167) and ZOL (10 μM, Abmole Bioscience, M5032). The cell viability
was evaluated using Cell Counting Kit-8 (Cck8, CK04, Dojindo, Japan)
after incubation for another twenty-four hours. For all the cultures,
media was changed every two days until indicated timepoints.

Lentivirus and plasmids transfection
Stat1-overexpression lentivirus (*HBLV-m-Stat1-HIS-ZsGreen-PURO*) with
its control lentivirus (*HBLV-ZsGreen-PURO*), and *Foxp1*-knockdown
lentivirus (*HBLV-m-Foxp1 shRNA1-NEO*) with its control lentivirus
(*HBLV-NEO NC*) were purchased from Hanbio Biotechnology Co. Ltd
(Shanghai). For lentivirus transfection, 2×10^5 Raw264.7 cells were
seeded in 12-well plates in α-MEM overnight and were infected with
lentivirus expressing either target gene or control lentivirus at a mul-
tiplicity of 20. After 24 h, transfected Raw264.7 cell line were induced
with 100 ng/ml RANKL for further test.

### Quantitative reverse transcription PCR (qPCR)
For qPCR analysis, RNA was extracted using TRIzol (Sigma, T9424) and
was reverse-transcribed with the Prime Script RT master kit (TakaRa
Bio Inc., RR036A). Then the relative amounts of each mRNA transcript
were analyzed using Roche LightCycler 480 system (v1.5.1.74) with
SsoAdvanced Universal SYBR Green Supermix (Bio-Rad, 1725270). The
expression of β-actin as an internal control. Primer sequences are listed
in Supplementary Table 2.

RNA-sequencing analysis
For RNA-sequencing analysis, libraries were prepared using NEBNext
Ultra II RNA Library Prep Kit and then sequenced on Illumina NovaSeq
6000 platform. Raw reads were filtered using Cutadapt (v1.15) and
aligned with the GRCm39 genome using HISAT2 v2.0.5. Read
Count values on each gene were compared using HTSeq (v0.9.1) and
normalized to FPKM. Then difference expression of genes was ana-
lyzed using DESeq (v1.30.0) (fold change > = 1.2 and $p < 0.05$) and R
language Pheatmap (v1.0.8) software package. GO enrichment analysis
of the different expressed genes was performed using topGO (v2.40.0)
($p < 0.05$). The enrichment analysis of the KEGG pathway of differential
genes was performed using ClusterProfiler (v3.4.4) software ($p < 0.05$).
GSEA analysis was performed to functionally annotate the
relevant genes and assess the enriched signaling pathways using
GSEA_Linux_4.1.0.

Western blot and co-immunoprecipitation (co-IP)
For western blot analysis, total protein was obtained and homogenized
in RIPA buffer (Cell Signaling, 9806 s) supplemented with protease
inhibitor (Thermo Fisher Scientific, A32959). Western blot was per-
formed per standard protocol and signals were detected using UVITEC
Alliance system (v16.0.3.0). Uncropped and unprocessed scans of the
blots are provided in the Source Data file. Antibodies used in western
blot as follows: BRD9 antibody (Abcam, ab259839, 1:1000), MMP9
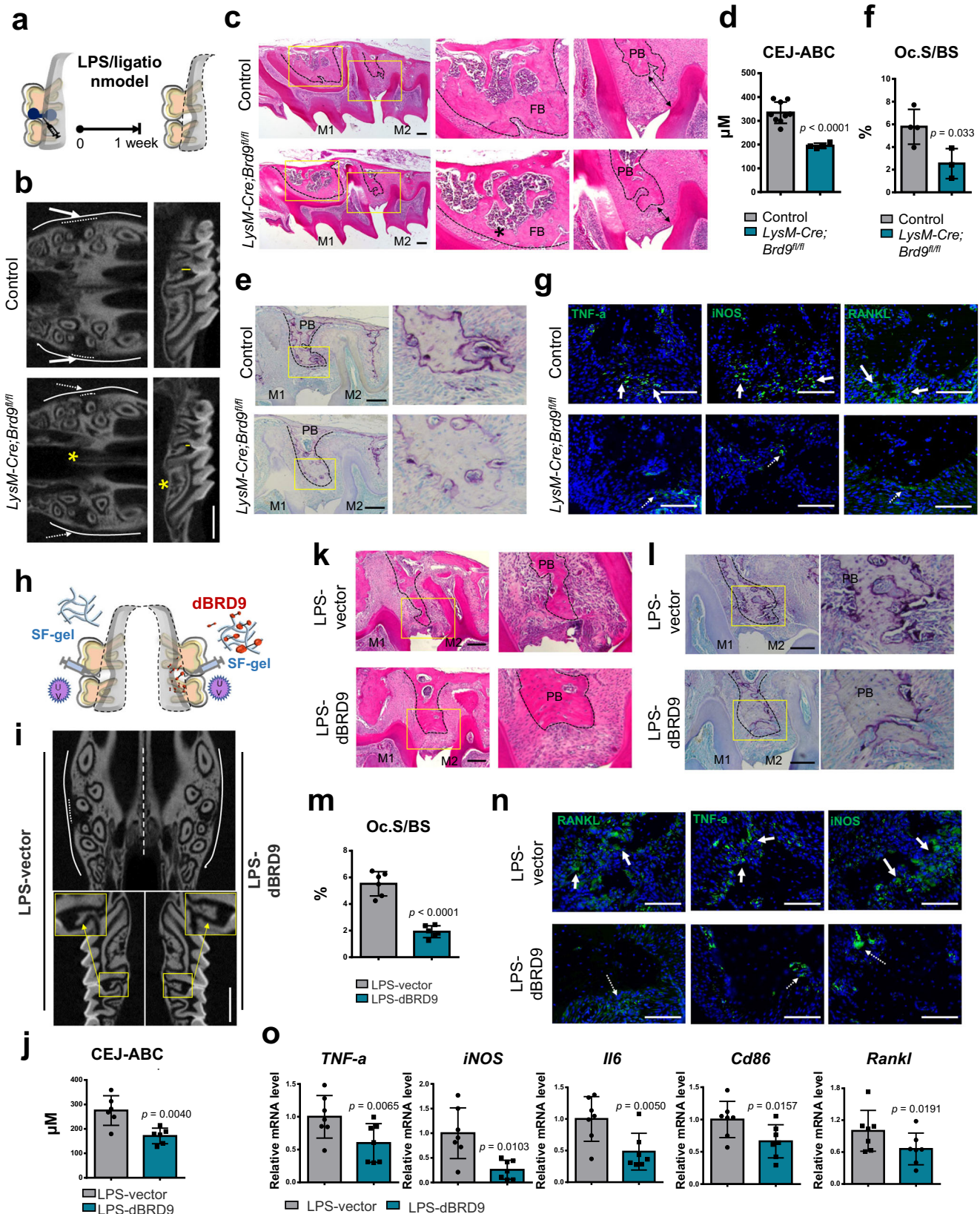
antibody (Abcam, ab228402, 1:1000), CTSK antibody (Abcam, ab37259, 1:1000), ACP5 antibody (Abcam, ab235448, 1:1000), β-actin antibody (Abcam, ab20272HRP, 1:5000), FOS antibody (Cell signaling, 4384, 1:1000), IFN-β1 antibody (Cell signaling, 97450, 1:1000), STAT2 antibody (Cell signaling, 72604, 1:1000), STAT1 antibody (Cell

signaling, 9172, 1:1000), FOXP1 antibody (Cell signaling, 4402, 1:1000), Mouse IgG HRP-conjugated antibody (R&D, HAF007, 1:1000) and Rabbit IgG HRP-conjugated antibody (R&D, HAF008, 1:1000).

For co-IP, BMDMs after osteoclast induction were harvested and lysed in Pierce™ IP Lysis Buffer (Thermo Fisher Scientific, 87787). Then

Fig. 9 | BRD9 deletion/degrader mitigates LPS-induced bone resorption.
a Schematic illustrating the protocol for establishing LPS-induced localized aggressive periodontitis (LAP). **b** μCT imaging and **d** quantification of LPS-induced local alveolar bone loss in the maxillary bone from 4-week-old *LysM-Cre;Brd9*$^{fl/fl}$ mice ($n = 4$) and littermate control mice ($n = 9$). Yellow line in **b** indicates cementum-enamel junction to alveolar bone crest (CEJ-ABC) distance (mm) in **d**. **c** H&E staining of LPS-stimulated maxillary bone from 4-week-old *LysM-Cre;Brd9*$^{fl/fl}$ mice and littermate control mice. Arrows indicate distance between gingival sulcus bottom to alveolar bone crest. **e** TRAP staining and **f** quantification of LPS-stimulated maxillary bone from 4-week-old *LysM-Cre;Brd9*$^{fl/fl}$ mice ($n = 3$) and littermate control mice ($n = 4$). **g** TNF-a, iNOS and RANKL immunofluorescence (green) in LPS-stimulated maxillary bone from 4-week-old *LysM-Cre;Brd9*$^{fl/fl}$ mice and littermate control mice. **h** Schematic illustrating dBRD9 degrader treatment. **i** μCT imaging and **j** quantification of LPS-induced local alveolar bone loss in BRD9 degrader treated (right) and control (left) lateral of the maxillary bone from 6-week-old mice. $n = 6$. **k** H&E staining, **l** TRAP staining, and **m** quantification of LPS-induced local alveolar bone in BRD9 degrader treated and control lateral of the maxillary bone from 6-week-old mice. $n = 6$. **n** RANKL, TNF-a, and iNOS immunofluorescence (green) in LPS-induced local alveolar bone in BRD9 degrader treated and control lateral of the maxillary bone from 6-week-old mice. **o** The mRNA expression of *TNF-a, iNOS, Il6, Cd86,* and *Rankl* of LPS-induced local alveolar bone in BRD9 degrader treated and control lateral of the maxillary bone from 6-week-old mice. $n = 7$. All data in this figure are represented as mean ± SD. Two-tailed Student's *t*-test for (**d**), (**f**), (**j**), (**m**), and (**o**). M1, first molar. M2, second molar. Asterisk in **b**, **c** indicates less bone mass. Scale bar in **b**, **i**, 1 mm; **c**, **e**, **k**, **l**, 200 μm; **g**, **n**, 100 μm. All experiments were performed in triplicates unless otherwise stated. Source data are provided in the Source data file.

lysates were subjected to immunoprecipitation with anti-FOXP1 antibody (Cell signaling, 4402, 1:200) or normal Rabbit IgG (Cell Signaling, 2729, 1:4000) and protein A-Sepharose (VWR, CA97067-898). Immune complexes were washed and subjected to immunoblotting with anti-FOXP1 (Cell signaling, 4402, 1:1000) or anti-BRD9 (Abcam, ab259839, 1:1000) antibodies.

Dual luciferase reporter assays
The predicted *Stat1* proximal promoter region (2.6 kb, −2995 ~ +576) and enhancer region (1.2 kb, −6338 ~ −5138) was synthesized and cloned into pGL3-basic luciferase reporter as and pGL3-basic-2.6 kb (promoter) and pGL3-basic-3.8 kb (promoter + enhancer). For transfection, 2×10^5 Raw264.7 cell line were seeded in 12-well plates in α-MEM overnight and were infected with above reporter clones using Lipofectamine 3000 transfection reagent (Thermo Fisher Scientific, L3000008) and Opti-MEM™ I Reduced Serum Medium (Thermo Fisher Scientific, 31985062) according to the manufacturer's protocol. After 24 h incubation, transfected Raw264.7 cell line were treated with iBRD9 or control vector cultured in presence of 100 ng/ml RANKL. After another 24 h incubation, the cell was lysed for dual luciferase reporter gene assay kit (Beyotime, RG027) according to the manufacturer's instructions. Renilla luciferase is used as an internal standard control, and the normalized reporter activity of all samples was compared. Each group had five replicate samples. Independent experiments were repeated in triplicate.

ATAC-sequencing analysis and motif analysis
5000 cells from each group of osteoclastic induced BMDMs treated with iBRD9 or control vector for 24 h were used for preparation of ATAC-seq libraries according to the protocol described by Kaestner Lab (https://www.med.upenn.edu/kaestnerlab/protocols.html). The transposed DNA libraries were sequenced on Illumina Novaseq 6000 system with PE150 mode. Library sequencing quality was assessed using Cutadapt (v1.9.1). Trimmed libraries were aligned to the GRCm39 mouse genome using Bowtie 2 (v2.2.6)[64]. PCR duplicates were removed and the number of mapped reads downsampled to a standard of ~20 M using Picard (v1.126) (http://broadinstitute.github.io/picard/). ATAC-Seq peaks were called subsequently using MACS (v3.0.0a6)[65] (-f BAMPE -B --SPMR –keep-dup all). Then the high-confidence set of peaks from all samples were merged to acquire consensus peakset. Potential DARs from consensus peakset were annotated with |log$_2$(fold change)| >= 0.5. Motif analysis on DARs was performed by MEME (v5.4.1) suite with default settings with $p < 0.01$[66]. Gene ontology enrichment was performed using R package ClusterProfiler (v4.6.0), with default settings.

ChIP assay and integrative analysis
BMDMs were osteoclastic induced in presence of 50 ng/ml M-CSF and 100 ng/ml RANKL for 3 days and fixed with formaldehyde after amplification for further ChIP-sequencing analysis. RAW264.7 cell were osteoclastic induced in presence of 100 ng/ml RANKL for 3 days and fixed with formaldehyde after amplification for further ChIP-qPCR analysis. The Simple ChIP Plus Enzymatic Chromatin IP Kit (Magnetic Beads; Cell Signaling Technology 9005), anti-FOXP1 antibody (Cell signaling, 4402, 1:100) with normal Rabbit IgG (Cell Signaling, 2729, 1:2000) as a non-specific IgG control, anti-BRD9 antibody (Bethyl Laboratories, A700-153, 1:100) with normal Rabbit IgG (Cell Signaling, 2729, 1:100) as a non-specific IgG control were used following the manufacturer's instructions. The *Stat1* ChIP primers for binding site 1 (BS1, −40 ~ +52) and binding site 2 (BS2, −5566 ~ −5424) amplified a region at the promoter and enhancer, respectively. Primer sequences are listed as follows. Stat1-BS1-F: AACAGCCGGCCAATCTCTG; Stat1-BS1-R: GAAAACCGAAAGTACCGGGC; Stat1-BS2-F: CCGGCTGAGTTCC-CAGAAAG; Stat1-BS2-R: AGGCTTTGCTTTAGGACCCC.

ChIP-sequencing libraries were prepared using the KAPA HTP Library Preparation Kit and were sequenced on Illumina Novaseq 6000 system. Double-end sequencing was used with 150 bp read length. Raw reads were filtered using FASTX-Toolkit (v0.0.14) (http://hannonlab.cshl.edu/fastx_toolkit/). Then the clean reads were aligned to the GRCm39 mouse genome using Bowtie 2 (v2.3.5.1)[64]. Multiple aligned reads were filtered out using Picard (v2.27.5) (http://broadinstitute.github.io/picard/). Then the unique mapped reads without duplicated reads were called for peaks using MACS2 (v2.2.71)[65] with default parameters and $p < 0.05$. The peaks were annotated using ChIPseeker (v1.20.0)[67] and motif analyses were carried out using the MEME (v4.1.2)[66].

For integrative analysis of RNA-Seq with ChIP-Seq, venn analysis was initially performed between the overlapping of RANKL-induced and iBRD9 downregulated genes (|log$_2$(fold change)| >= 0.1 and $p < 0.05$) using the RNA-sequencing datasets. And the overlapping genes were further compared with the BRD9 binding profiles during osteoclastogenesis using Venn analysis. Then, KEGG enrichment and PPI analysis were conducted with the overlapping 717 genes where BRD9 binding, RANKL-induced while downregulated after BRD9 inhibition. To identify potential interacting TFs of BRD9 during osteoclastogenesis, the top enriched loss motifs after BRD9 inhibition using the ATAC-seq data and the BRD9 binding sites enriched motifs using the ChIP-seq data were further integrative analyzed.

Statistical and reproducibility
All statistical analyses were performed with GraphPad Prism v6.01 software and are presented as mean ± standard deviation. Unpaired two-tailed t-test between two groups or one-way analysis of variance (ANOVA) with Tukey's or Dunnett's multiple comparisons post hoc test among three or more groups was used for comparisons. $P < 0.05$ is considered statistically significant. All experiments were repeated in triplicate or more unless otherwise stated.

Reporting summary
Further information on research design is available in the Nature Portfolio Reporting Summary linked to this article.

Data availability

The mRNA, ATAC, and ChIP-sequencing data generated in this study have been deposited in the Gene Expression Omnibus database under accession code GSE222240. GRCm39 genome is referenced in this study [http://asia.ensembl.org/Mus_musculus/Info/Index]. The other relevant data generated in this study are provided in the Supplementary Information/Source data file. Source data are provided with this paper.

References

1. Sobacchi, C., Schulz, A., Coxon, F. P., Villa, A. & Helfrich, M. H. Osteopetrosis: genetics, treatment and new insights into osteoclast function. *Nat. Rev. Endocrinol.* **9**, 522–536 (2013).
2. Soltanoff, C. S., Yang, S., Chen, W. & Li, Y. P. Signaling networks that control the lineage commitment and differentiation of bone cells. *Crit. Rev. Eukaryot. Gene Expr.* **19**, 1–46 (2009).
3. Asagiri, M. & Takayanagi, H. The molecular understanding of osteoclast differentiation. *Bone* **40**, 251–264 (2007).
4. An, E., Narayanan, M., Manes, N. P. & Nita-Lazar, A. Characterization of functional reprogramming during osteoclast development using quantitative proteomics and mRNA profiling. *Mol. Cell Proteom.* **13**, 2687–2704 (2014).
5. Alfert, A., Moreno, N. & Kerl, K. The BAF complex in development and disease. *Epigenetics Chromatin* **12**, 19 (2019).
6. Mashtalir, N. et al. A structural model of the endogenous human BAF complex informs disease mechanisms. *Cell* **183**, 802–817.e824 (2020).
7. Alver, B. H. et al. The SWI/SNF chromatin remodelling complex is required for maintenance of lineage specific enhancers. *Nat. Commun.* **8**, 14648 (2017).
8. Han, L. et al. ARID1A is critical for maintaining normal hematopoiesis in mice. *Blood* **132**, 3833–3833 (2018).
9. Gatchalian, J. et al. A non-canonical BRD9-containing BAF chromatin remodeling complex regulates naive pluripotency in mouse embryonic stem cells. *Nat. Commun.* **9**, 5139 (2018).
10. Weisberg, E. et al. BRD9 degraders as chemosensitizers in acute leukemia and multiple myeloma. *Blood Cancer J.* **12**, 110 (2022).
11. Del Gaudio, N. et al. BRD9 binds cell type-specific chromatin regions regulating leukemic cell survival via STAT5 inhibition. *Cell Death Dis.* **10**, 338 (2019).
12. Ahmed, N. S. et al. BRD9 regulates interferon-stimulated genes during macrophage activation via cooperation with BET protein BRD4. *Proc. Natl Acad. Sci. USA* **119**, e2110812119 (2022).
13. Wang, L. et al. Bromodomain containing 9 (BRD9) regulates macrophage inflammatory responses by potentiating glucocorticoid receptor activity. *Proc. Natl Acad. Sci. USA* **118**, e2109517118 (2021).
14. Theodoulou, N. H. et al. Discovery of I-BRD9, a selective cell active chemical probe for bromodomain containing protein 9 inhibition. *J. Med Chem.* **59**, 1425–1439 (2016).
15. Wei, Z. et al. Vitamin D switches BAF complexes to protect beta. *Cells Cell* **173**, 1135–1149.e1115 (2018).
16. McComb, S. et al. Type-I interferon signaling through ISGF3 complex is required for sustained Rip3 activation and necroptosis in macrophages. *Proc. Natl Acad. Sci. USA* **111**, E3206–E3213 (2014).
17. Takayanagi, H. et al. RANKL maintains bone homeostasis through c-Fos-dependent induction of interferon-beta. *Nature* **416**, 744–749 (2002).
18. Takuma, A. et al. Dexamethasone enhances osteoclast formation synergistically with transforming growth factor-beta by stimulating the priming of osteoclast progenitors for differentiation into osteoclasts. *J. Biol. Chem.* **278**, 44667–44674 (2003).
19. Seeliger, C. et al. Signaling pathway STAT1 is strongly activated by IFN-beta in the pathogenesis of osteoporosis. *Eur. J. Med. Res.* **20**, 1 (2015).
20. Sun, G. J. et al. Significant pathways detection in osteoporosis based on the bibliometric network. *Eur. Rev. Med. Pharm. Sci.* **17**, 1–7 (2013).
21. Place, D. E. et al. Osteoclast fusion and bone loss are restricted by interferon inducible guanylate binding proteins. *Nat. Commun.* **12**, 496 (2021).
22. Caputo, V. S. et al. Brd2/4 and Myc regulate alternative cell lineage programmes during early osteoclast differentiation in vitro. *iScience* **24**, 101989 (2021).
23. Yuasa, K. & Hijikata, T. Distal regulatory element of the STAT1 gene potentially mediates positive feedback control of STAT1 expression. *Genes Cells* **21**, 25–40 (2016).
24. Liu, Z. et al. Two novel STAT1 mutations cause Mendelian susceptibility to mycobacterial disease. *Biochem Biophys. Res. Commun.* **591**, 124–129 (2022).
25. Noma, K., Mizoguchi, Y., Tsumura, M. & Okada, S. Mendelian susceptibility to mycobacterial diseases: state of the art. *Clin. Microbiol. Infect.* **28**, 1429–1434 (2022).
26. Du, J. et al. Arid1a-Plagl1-Hh signaling is indispensable for differentiation-associated cell cycle arrest of tooth root progenitors. *Cell Rep.* **35**, 108964 (2021).
27. Chandler, R. L. et al. ARID1a-DNA interactions are required for promoter occupancy by SWI/SNF. *Mol. Cell Biol.* **33**, 265–280 (2013).
28. Alpsoy, A. et al. BRD9 is a critical regulator of androgen receptor signaling and prostate cancer progression. *Cancer Res.* **81**, 820–833 (2021).
29. Zhao, H. et al. Integrative bone metabolomics-lipidomics strategy for pathological mechanism of postmenopausal osteoporosis mouse model. *Sci. Rep.* **8**, 16456 (2018).
30. Irie, A., Yamamoto, K., Miki, Y. & Murakami, M. Phosphatidylethanolamine dynamics are required for osteoclast fusion. *Sci. Rep.* **7**, 46715 (2017).
31. Wang, L. et al. Dopamine suppresses osteoclast differentiation via cAMP/PKA/CREB pathway. *Cell Signal* **78**, 109847 (2021).
32. Konopacki, C., Pritykin, Y., Rubtsov, Y., Leslie, C. S. & Rudensky, A. Y. Transcription factor Foxp1 regulates Foxp3 chromatin binding and coordinates regulatory T cell function. *Nat. Immunol.* **20**, 232–242 (2019).
33. Shi, C. et al. Down-regulation of the forkhead transcription factor Foxp1 is required for monocyte differentiation and macrophage function. *Blood* **112**, 4699–4711 (2008).
34. Makin, S. The destructive power of PROTACs could tackle prostate cancer. *Nature* **609**, S41 (2022).
35. Remillard, D. et al. Degradation of the BAF complex factor BRD9 by heterobifunctional ligands. *Angew. Chem. Int. Ed. Engl.* **56**, 5738–5743 (2017).
36. Anesi, A., Generali, L., Sandoni, L., Pozzi, S. & Grande, A. From osteoclast differentiation to osteonecrosis of the jaw: molecular and clinical insights. *Int. J. Mol. Sci.* **20**, 4925 (2019).
37. Zhu, W. et al. Zoledronic acid promotes TLR-4-mediated M1 macrophage polarization in bisphosphonate-related osteonecrosis of the jaw. *FASEB J.* **33**, 5208–5219 (2019).
38. Brien, G. L. et al. Targeted degradation of BRD9 reverses oncogenic gene expression in synovial sarcoma. *Elife* **7**, e41305 (2018).
39. Bi, Y. et al. Bisphosphonates cause osteonecrosis of the jaw-like disease in mice. *Am. J. Pathol.* **177**, 280–290 (2010).
40. Rockwood, D. N. et al. Materials fabrication from Bombyx mori silk fibroin. *Nat. Protoc.* **6**, 1612–1631 (2011).
41. Qiao, W. et al. SARS-CoV-2 infection induces inflammatory bone loss in golden Syrian hamsters. *Nat. Commun.* **13**, 2539 (2022).
42. Yasui, T. et al. Epigenetic regulation of osteoclast differentiation: possible involvement of Jmjd3 in the histone demethylation of Nfatc1. *J. Bone Min. Res.* **26**, 2665–2671 (2011).
43. Inoue, K. & Imai, Y. Identification of novel transcription factors in osteoclast differentiation using genome-wide analysis of open

chromatin determined by DNase-seq. *J. Bone Min. Res.* **29**, 1823–1832 (2014).

44. Yi, S. J. et al. The KDM4B-CCAR1-MED1 axis is a critical regulator of osteoclast differentiation and bone homeostasis. *Bone Res.* **9**, 27 (2021).

45. Wang, X. et al. BRD9 defines a SWI/SNF sub-complex and constitutes a specific vulnerability in malignant rhabdoid tumors. *Nat. Commun.* **10**, 1881 (2019).

46. Mair, N. K. & Hale, B. G. Ultra-rare BRD9 loss-of-function variants limit the antiviral action of interferon. *Sci. Rep.* **12**, 15360 (2022).

47. Borold, J. et al. BRD9 is a druggable component of interferon-stimulated gene expression and antiviral activity. *EMBO Rep.* **22**, e52823 (2021).

48. Choudhary, C., Weinert, B. T., Nishida, Y., Verdin, E. & Mann, M. The growing landscape of lysine acetylation links metabolism and cell signalling. *Nat. Rev. Mol. Cell Biol.* **15**, 536–550 (2014).

49. Morgado-Pascual, J. L., Rayego-Mateos, S., Tejedor, L., Suarez-Alvarez, B. & Ruiz-Ortega, M. Bromodomain and extraterminal proteins as novel epigenetic targets for renal diseases. *Front Pharm.* **10**, 1315 (2019).

50. Baud'huin, M. et al. Inhibition of BET proteins and epigenetic signaling as a potential treatment for osteoporosis. *Bone* **94**, 10–21 (2017).

51. Liu, Y. et al. A novel BRD4 inhibitor suppresses osteoclastogenesis and ovariectomized osteoporosis by blocking RANKL-mediated MAPK and NF-kappaB pathways. *Cell Death Dis.* **12**, 654 (2021).

52. Park-Min, K. H. et al. Inhibition of osteoclastogenesis and inflammatory bone resorption by targeting BET proteins and epigenetic regulation. *Nat. Commun.* **5**, 5418 (2014).

53. Lamoureux, F. et al. Selective inhibition of BET bromodomain epigenetic signalling interferes with the bone-associated tumour vicious cycle. *Nat. Commun.* **5**, 3511 (2014).

54. Devaiah, B. N. et al. BRD4 is a histone acetyltransferase that evicts nucleosomes from chromatin. *Nat. Struct. Mol. Biol.* **23**, 540–548 (2016).

55. Stratton, M. S. et al. Signal-dependent recruitment of BRD4 to cardiomyocyte super-enhancers is suppressed by a microRNA. *Cell Rep.* **16**, 1366–1378 (2016).

56. Liu, B. et al. BRD4-directed super-enhancer organization of transcription repression programs links to chemotherapeutic efficacy in breast cancer. *Proc. Natl Acad. Sci. USA* **119**, e2109133119 (2022).

57. Braccioli, L. et al. FOXP1 promotes embryonic neural stem cell differentiation by repressing Jagged1 expression. *Stem Cell Rep.* **9**, 1530–1545 (2017).

58. Liu, X. M., Du, S. L., Miao, R., Wang, L. F. & Zhong, J. C. Targeting the forkhead box protein P1 pathway as a novel therapeutic approach for cardiovascular diseases. *Heart Fail Rev.* **27**, 345–355 (2022).

59. Li, H. et al. FOXP1 controls mesenchymal stem cell commitment and senescence during skeletal aging. *J. Clin. Invest.* **127**, 1241–1253 (2017).

60. Zervos, A. S., Gyuris, J. & Brent, R. Mxi1, a protein that specifically interacts with Max to bind Myc-Max recognition sites. *Cell* **72**, 223–232 (1993).

61. Kodric, K. et al. Sex-determining region Y (SRY) attributes to gender differences in RANKL expression and incidence of osteoporosis. *Exp. Mol. Med.* **51**, 1–16 (2019).

62. Madisen, L. et al. A robust and high-throughput Cre reporting and characterization system for the whole mouse brain. *Nat. Neurosci.* **13**, 133–140 (2010).

63. Du, J. H. et al. The function of wnt ligands on osteocyte and bone remodeling. *J. Dent. Res.* **98**, 930–938 (2019).

64. Langmead, B. & Salzberg, S. L. Fast gapped-read alignment with Bowtie 2. *Nat. Methods* **9**, 357–359 (2012).

65. Zhang, Y. et al. Model-based analysis of ChIP-Seq (MACS). *Genome Biol.* **9**, R137 (2008).

66. Bailey, T. L. et al. MEME SUITE: tools for motif discovery and searching. *Nucleic Acids Res.* **37**, W202–W208 (2009).

67. Yu, G. W.L.a.H.Q. ChIPseeker: an R/Bioconductor package for ChIP peak annotation, comparison and visualization. *Bioinformatics* **31**, 2382–2383 (2015).

Acknowledgements

Author contributions
J.D. and X.J. conceived and designed the study; J.D., Y.L., X.W., J. Sun., H.Z., A.Z., and M.Z. performed the experiments; M.Z. provided critical resources; J. Shi. analyzed the sequencing data; M.Z. and X.J. provided technical assistance and supervision; all authors contributed to the interpretation of experiments. J.D., Y.L., X.W., M.Z., and X.J. wrote the paper with input from all co-authors. J.D. and X.J. provided funding and supervision.

Competing interests
The authors declare no competing interests.

Additional information
Supplementary information The online version contains supplementary material available at https://doi.org/10.1038/s41467-023-37116-5.

Correspondence and requests for materials should be addressed to Mingliang Zhou or Xinquan Jiang.

Peer review information *Nature Communications* thanks the other anonymous reviewer(s) for their contribution to the peer review of this work.

Reprints and permissions information is available at http://www.nature.com/reprints

Publisher's note Springer Nature remains neutral with regard to jurisdictional claims in published maps and institutional affiliations.